Analytic model for the bispectrum of galaxies in redshift space

Smith, R E ; Sheth, R K ; Scoccimarro, R

Abstract: We develop an analytic theory for the redshift space bispectrum of dark matter, haloes and galaxies. This is done within the context of the halo model of structure formation, as this allows for the self-consistent inclusion of linear and non-linear redshift space distortions and also for the non-linearity of the halo bias. The model is applicable over a wide range of scales: on the largest scales the predictions reduce to those of the standard perturbation theory (PT); on smaller scales they are determined primarily by the nonlinear virial velocities of galaxies within haloes, and this gives rise to the U-shaped anisotropy in the reduced bispectrum – a finger print of the Finger-Of-God distortions. We then confront the predictions with bispectrum measurements from an ensemble of numerical simulations. On very large scales, k=0.05 h/Mpc, we find reasonably good agreement between our Halo Model, PT and the data, to within the errors. On smaller scales, k=0.1 h/Mpc, the measured bispectra differ from the PT at the level of 10-20%, especially for colinear triangle configurations. The Halo Model predictions improve over PT, but are accurate to no better than 10%. On smaller scales k=0.5-1.0 h/Mpc, our model provides a significant improvement over PT, which breaks down. This implies that studies which use the lowest order PT to extract galaxy bias information are not robust on scales k>0.1 h/Mpc. The analytic and simulation results also indicate that there is no observable scale for which the configuration dependence of the reduced bispectrum is constant–hierarchical models for the higher order correlation functions in redshift space are unlikely to be useful. It is hoped that our model will facilitate extraction of information from large-scale structure surveys of the Universe.

DOI: https://doi.org/10.1103/PhysRevD.78.023523

An analytic model for the bispectrum of galaxies in redshift space

Robert E. Smith[1,2], Ravi K. Sheth[1] and Román Scoccimarro[3]

(1) University of Pennsylvania, 209 South 33rd Street, Philadelphia, PA 19104, USA.
(2) Institute für Theoretical Physik, University of Zürich, Zürich, CH8051, Switzerland
(3) CCPP, Department of Physics, New York University, New York, NY 10003, USA.

email: res@physik.unizh.ch, shethrk@physics.upenn.edu, rs123@nyu.edu,

(Dated: December 29, 2010)

We develop the analytic theory for the redshift space bispectrum of galaxies, and present the methodology for making predictions of the redshift space galaxy 3-point correlation function. We use the framework of the halo model as this allows self-consistent inclusion of redshift space distortions and non-linear halo biasing with perturbation theory (PT) methods. The model shows that the U-shaped anisotropy on small scales is essentially a finger print of the Finger-Of-God distortions. It also shows that there is *no* observable scale for which the configuration dependence of the bispectrum is constant—hierarchical models for the higher order correlation functions in redshift space are unlikely to be useful. We then confront our analytic model with measurements of the nonlinear bispectrum from simulations. We find that on large scales, $k = 0.1\,h\mathrm{Mpc}^{-1}$, whilst both the PT and halo model predict the correct configuration dependence, the amplitudes are roughly $\sim 20\%$ too high. This implies that studies which use the lowest order PT to extract galaxy bias are unlikely to be robust on these scales – higher order terms in the PT will be necessary for good agreement. For higher wavenumbers $k = 0.5\,h\mathrm{Mpc}^{-1}$, our analytic model matches well the measurements, significantly improving on the PT model. We hope that our approach will help to facilitate extraction of information from current and future hi-fidelity large scale structure surveys of the Universe, because different galaxy populations are easily and naturally included into our description.

PACS numbers: 98.80.-k

I. INTRODUCTION

Statistical analyses of the large scale structures observed in galaxy surveys can provide a wealth of information about the cosmological parameters, the underlying mass distribution and the initial conditions of the Universe[1, 2, 3, 4, 5]. Some complex combination of the information is commonly extracted through measurement of the two-point correlation function, or it's Fourier space analogue the power spectrum. Since the evolved density field of galaxies is highly non-Gaussian, further complementary information is contained within the higher order clustering statistics [6]. For example, analysis of the large-scale 3-point correlation function, or its Fourier space dual the bispectrum, on large scales, can: test the non-linearity of bias – the way in which an observable tracer distribution samples the unobservable distribution of physical interest [7, 8, 9, 13]; constrain our hypothesis of Gaussianity in the initial conditions [10, 11, 12, 14]; break degeneracies between parameters, hence allowing improved constraints on the amplitude of the matter power spectrum; and also the higher order statistics have been highlighted as an important piece of solving the puzzle as to whether the observed accelerated expansion of the Universe is due to Dark Energy physics or a modification to gravity [15, 16, 17, 18]. On smaller scales these statistics can be most usefully used as a discriminator for the shapes of haloes [19] – and thus have the potential to constrain the small-scale dark matter physics.

The current state of the art galaxy redshift surveys [20, 21, 22, 23] have provided large samples of the Universe, and investigators have already carried out some of the tests noted above: 3-point correlation functions have been estimated by[24, 25, 26, 27, 28, 29] and bispectra by [30, 31, 32].

Current theoretical modeling of the large scale bispectrum rests on results from perturbation theory and non-linear biasing in real (as opposed to redshift) space. In the large scale limit, this gives rise to a simple model [7, 8, 9]:

$$Q^{\rm g}(k_1,k_2,\theta_{12}) = \frac{1}{b_1^{\rm g}}\left[Q^{\rm m}(k_1,k_2,\theta_{12}) + c_2^{\rm g}\right] \ ; \qquad (1)$$

where the functions Q^i are the reduced bispectra of galaxies and matter, $Q^i_{123} \equiv B^i_{123}/\left[P^i_1P^i_2 + P^i_2P^i_3 + P^i_3P^i_1\right]$. In the above $B_{123} \equiv B(k_1,k_2,\theta_{12})$ is the matter bispectrum and $P_a \equiv P(k_a)$ the matter power spectrum. The coefficient $b_1^{\rm g}$ is the large scale linear bias parameter and $c_2^{\rm g} \equiv b_2^{\rm g}/b_1^{\rm g}$ is the first non-linear bias parameter. It is usually assumed that this relation holds in redshift space as well, but that it does not in detail can be seen from the work of [33]. That it nevertheless appears to be a reasonable working hypothesis was demonstrated by [34]. We shall, hereafter, refer to this model in real and redshift space as PT and PTs, respectively.

There are several reasons why we wish to improve upon PTs. Firstly, it is well known that in redshift space the distortion effects from non-linear structures, such as Finger-of-God (hereafter FOG) distortions, pollute the scales that are usually identified for linear treatment. This can not be accounted for in the perturbation

theory in any other way than supposing 'ad-hoc' fixes to the model [33, 35]. A pragmatist might argue that one may take scales that are sufficiently large that these corrections can be neglected. However, even if we are proficient enough to accurately separate linear from non-linear scales, then we are still faced with loosing a significant amount of information from our data through the restrictions to very large scales. Therefore some means for robustly modeling the FOG effects is clearly of great value as this may allow us to expand the utility of our data set and improve precision.

Secondly, in our study of the large scale galaxy power spectrum [36] we found that there was non-trivial scale dependence arising from non-linear bias and gravitational mode coupling, even on the largest scales currently probed. One may then ask how these properties affect the predicted bispectra.

In this paper we concentrate on building a new analytic model for the fully non-linear redshift space bispectrum. We work in the context of the halo model [37], since it naturally affords a means for including linear and non-linear density and velocity information [38, 39, 40, 41, 42] and neatly allows for the inclusion of galaxies [38, 43, 44, 45, 46, 47]. Furthermore, as was shown in [36] the halo model presents a natural framework for understanding the origins of the non-linear scale dependence of bias. However, the limitations of the halo model predictions for precision measurements of the matter power spectrum on large scales have been known for some time now [37, 48, 49, 50] – the case being most clearly exposed by [49]. However, it is not yet clear how important these failings are for galaxy clustering – since the dynamics of the galaxies do not have to conserve momentum. We will therefore use measurements from numerical simulations, to confirm the validity of our predictions.

We shall also wish to construct a model for the redshift space 3-point correlation function, without requiring substantial additional effort. In this respect, the duality of Eq. (1), by which we mean the property that it takes the same form in Configuration and Fourier space (see Appendix A for further details) is an attractive feature that we would like to replicate in any new formulation – but it may be that adding more realism to the model cannot be done in a trivial way. We therefore present a general methodology for how one should recover the 3-point function from our model but leave it to future work to show that this can be practically implemented.

The paper breaks up as follows: In Section II we formalize the halo model in redshift space, providing general expressions for the 3-point function and bispectrum. Section III details the necessary components of the model; we pay special attention to the redshift-space clustering of halo centers. Section IV presents the central analytic result of the paper—a calculation of the isotropic bispectrum. Some results of evaluating our expressions are presented in Section V. In Section VI we confront our model with measurements from N-body simulations. In Section VII we use a spherical harmonic expansion to show how the redshift space 3-point correlation function may be obtained from our calculation of the redshift space bispectrum. A final section discusses our results and draws conclusions.

Although our analysis is general, we shall illustrate our results with specific examples. When necessary, we assume a flat Friedmann-Lemaître-Robertson-Walker (FLRW) cosmological model with energy density at late times dominated by a cosmological constant (Λ) and a sea of collisionless cold dark matter particles as the dominant mass density. We set $\Omega_m = 0.27$ and $\Omega_\Lambda = 0.73$, where these are the ratios of the energy density in matter and a cosmological constant to the critical density, respectively. We use a linear theory power spectrum generated from `cmbfast`[51], with baryon content of $\Omega_b = 0.046$ and $h = 0.72$. The normalization of fluctuations is set through $\sigma_8 = 0.9$, which is the r.m.s. variance of fluctuations in spheres of radius $8h^{-1}\,\mathrm{Mpc}$.

II. HALO MODEL IN REDSHIFT SPACE

A. Formalism

In the halo model (see [37] for a review) the density field is decomposed into a set of dark matter haloes, where a halo is defined to be a region that has undergone gravitational collapse forming a dense virialized ball of cold dark matter (CDM). All statistical quantities of interest are then considered as sums over the halo distribution. Thus to understand the large scale clustering of a distribution of objects, haloes, galaxies or dark matter, we simply require understanding of how the haloes themselves cluster; the different tracer types simply act as weights. In particular, different galaxy populations 'weight' haloes differently: the Halo Occupation Distribution (HOD) [43, 44, 45, 46, 47], specifies how the probability for obtaining N galaxies depends on halo mass M. To model redshift space statistics, we require additional information about how the large scale velocity field modifies the halo clustering, as well as a model for the distribution function of galaxy velocities within each halo. The halo model in redshift space , at the two-point level, was developed by [39, 40, 41] (hereafter we shall refer to the Halo model in real and redshift space as HM and HMs, respectively). However, some unresolved issues remained with regard to the base formalism. These were resolved by [42] and our description of 3-point statistics presented here extends these analyses. For completeness some of these details are repeated below.

The density field of dark matter, haloes or galaxies may be written as

$$\rho^s_\alpha(\mathbf{s}) = \sum_i [W_\alpha]_i \, U^s_{\alpha,i}(\mathbf{s} - \mathbf{s}_i | M_i) \; , \tag{2}$$

where $\alpha = \{1, 2, 3\}$ refers to the particular choice of weight for the ith halo in the sum, i.e. $[W_\alpha]_i =$

$\{1, M_i, N^{\rm g}(M_i), \dots\}$ depending on the spectra one wishes to model, and where $N^{\rm g}(M_i)$ is the number of galaxies in halo i. $U^s_{\alpha,i}$ is the normalized density distribution of objects in redshift space within the ith halo. In this paper we shall always assume that $U^s_{\alpha,i} \equiv \rho^s(\mathbf{s})/M$, is the mass-normalized density profile of dark matter in redshift space, although our formalism does not rely upon this assumption and may readily be generalized for more complicated mass distributions. At this point the only difference between Eq. (2) and the real space density field, is that we have used $\mathbf{s}$ to denote comoving spatial positions. However this has the special meaning that Hubble's law, $\mathbf{v} = H(a)\mathbf{r}$, is used to infer proper radial positions from recession velocities, where $\mathbf{v}$ is the proper velocity, $H(a) \equiv \dot{a}/a$ is the Hubble parameter and $\mathbf{r}$ is the proper separation (related to comoving coordinate through $\mathbf{r} = a\,\mathbf{x}$). The notion of redshift space distortions then follow from the fact that objects which form through gravitational instability acquire a local peculiar velocity of their own, and hence the velocity–space mapping in general is non-linear. In this paper we shall work in *the plane parallel approximation*, where observed structures are located at infinity. Then the mapping is

$$s_z = z - u_z(\mathbf{x}) \;;\; \mathbf{s}_\perp = \mathbf{x}_\perp \tag{3}$$

where u_z is the comoving peculiar velocity, scaled in units of the Hubble parameter; we take this to be negative for convenience.

B. Higher order correlations

We may now compute the correlation hierarchy for such a distribution of tracer objects. For a definition of the higher-order clustering statistics in configuration space and their Fourier space dual counterparts we refer to Appendix A. There may also be found useful symmetry properties that we exploit throughout.

Following [19, 37, 46, 52, 53], the real-space 3-point correlation function (ζ^s_α) in the halo model, for dark matter, haloes or galaxies, is the sum of three terms: the first represents the case where all three points in space are contained in a single halo; the second is the case where two points are located in one halo and the third is in a separate halo; the third is the case where three points are located in three distinct haloes – we shall refer to these as the 1-, 2- and 3-Halo terms and ($\zeta^s_{\alpha,1\rm H}$, $\zeta^s_{\alpha,2\rm H}$, $\zeta^s_{\alpha,3\rm H}$). These are written:

$$\zeta^s_\alpha(\mathbf{s}_1,\mathbf{s}_2,\mathbf{s}_3) \equiv \zeta^s_{\alpha,1\rm H}(\mathbf{s}_1,\mathbf{s}_2,\mathbf{s}_3) + \zeta^s_{\alpha,2\rm H}(\mathbf{s}_1,\mathbf{s}_2,\mathbf{s}_3) + \zeta^s_{\alpha,3\rm H}(\mathbf{s}_1,\mathbf{s}_2,\mathbf{s}_3) \;\; ; \tag{4}$$

$$\zeta^s_{\alpha,1\rm H}(\mathbf{s}_1,\mathbf{s}_2,\mathbf{s}_3) = \frac{1}{\bar{\rho}^3_\alpha}\int dM\; d^3y\; [W_\alpha]^3\; n(M) \prod_{i=1}^{3}\Big\{\; U^s(\mathbf{y}-\mathbf{s}_i|M)\Big\} \;\; ; \tag{5}$$

$$\zeta^s_{\alpha,2\rm H}(\mathbf{s}_1,\mathbf{s}_2,\mathbf{s}_3) = \frac{1}{\bar{\rho}^3_\alpha}\int \prod_{i=\{1,2\}}\Big\{\; dM_i\; d^3y_i\; [W_\alpha]_i\, n(M_i)\; U^s(\mathbf{y}_i-\mathbf{s}_i|M_i)\Big\}\; [W_\alpha]_1\; U^s(\mathbf{y}_1-\mathbf{s}_3|M_1)$$
$$\times\;\; \xi^s_{\rm hc}(\mathbf{y}_1,\mathbf{y}_2|M_1,M_2) + \text{cyc} \;; \tag{6}$$

$$\zeta^s_{\alpha,3\rm H}(\mathbf{s}_1,\mathbf{s}_2,\mathbf{s}_3) = \frac{1}{\bar{\rho}^3_\alpha}\int \prod_{i=1}^{3}\Big\{\; dM_i\; d^3y_i\; [W_\alpha]_i\, n(M_i)\, U^s(\mathbf{y}_i-\mathbf{s}_i|M_i)\Big\}\, \zeta^s_{\rm hc}(\mathbf{y}_1,\mathbf{y}_2,\mathbf{y}_3|M_1,M_2,M_3) \;\; , \tag{7}$$

where $\xi^s_{\rm hc}$ and $\zeta^s_{\rm hc}$ are the 2- and 3-point correlation functions of halo centers, conditioned on halo masses and where $n(M)dM$ is the halo mass function, which gives the number density of dark matter haloes with masses in the range M to $M + dM$.

The inverse Fourier transforms of these 3-point functions are the redshift space bispectra (c.f. Eq. A18). They are written:

$$B^s_\alpha(\mathbf{k}_1,\mathbf{k}_2,\mathbf{k}_3) = B^s_{\alpha,1\rm H}(\mathbf{k}_1,\mathbf{k}_2,\mathbf{k}_3) + B^s_{\alpha,2\rm H}(\mathbf{k}_1,\mathbf{k}_2,\mathbf{k}_3) + B^s_{\alpha,3\rm H}(\mathbf{k}_1,\mathbf{k}_2,\mathbf{k}_3)\ , \quad (8)$$

$$B^s_{\alpha,1\rm H}(\mathbf{k}_1,\mathbf{k}_2,\mathbf{k}_3) = \frac{1}{\bar\rho^3_\alpha}\int dM\,[W_\alpha]^3\,n(M)\prod_{i=1}^{3}\Big\{\,U^s(\mathbf{k}_i|M)\Big\}\ , \quad (9)$$

$$B^s_{\alpha,2\rm H}(\mathbf{k}_1,\mathbf{k}_2,\mathbf{k}_3) = \frac{1}{\bar\rho^3_\alpha}\int \prod_{i=\{1,2\}}\Big\{\,dM_i\,[W_\alpha]_i\,n(M_i)U^s(\mathbf{k}_i|M_i)\Big\}\,[W_\alpha]_1\,U^s(\mathbf{k}_3|M_1)P^s_{\rm hc}(\mathbf{k}_2|M_1,M_2) + \text{cyc}\ , \quad (10)$$

$$B^s_{\alpha,3\rm H}(\mathbf{k}_1,\mathbf{k}_2,\mathbf{k}_3) = \frac{1}{\bar\rho^3_\alpha}\int \prod_{i=1}^{3}\Big\{\,dM_i\,[W_\alpha]_i\,n(M_i)\,U^s(\mathbf{k}_i|M_i)\Big\}\,B^s_{\rm hc}(\mathbf{k}_1,\mathbf{k}_2,\mathbf{k}_3|M_1,M_2,M_3)\ , \quad (11)$$

where $P^s_{\rm hc}$ and $B^s_{\rm hc}$ are the Fourier transforms of the 2- and 3-point halo center correlation functions.

Several advantages are gained from transforming to Fourier space. Firstly, once the integrals over mass are included, $\zeta^s_{3\rm H}$ requires evaluation of a 12-D integral—the corresponding term $B^s_{3\rm H}$ is significantly simpler. Indeed, for the case of real space – not redshift space – and for spherical haloes, it is possible to write $B_{3\rm H}$ as the product of 3 2-D integrals. The calculation is slightly more complicated in redshift space but, as we show below, it remains tractable. Thus, to compute the redshift space power spectrum and bispectrum, we require three components: the abundance of dark matter haloes $n(M)$; a model for the redshift space density profile; and a model for the inter-clustering of dark matter haloes in redshift space. In the following sections we describe our choices for these quantities.

III. INGREDIENTS

A. Halo abundances and bias factors

The halo mass function $n(M)$ plays a central role in the halo model. It has been the subject of much detailed study [54, 55, 56, 57]. These studies suggest that, in appropriately scaled units, halo abundances should be approximately independent of cosmology, power spectrum and redshift. These models for $n(M)$ also predict that the real-space clustering of halos should be biased relative to that of the dark matter [56]; the way in which real-space halo bias depends on halo mass is related to the shape of $n(M)$. Thus, once the mass function has been specified, the problem of describing halo clustering reduces to one of describing the clustering of the dark matter. Of the many recent parametrizations of $n(M)$, [56, 58, 59, 60], we use that of Sheth & Tormen [56]. Changing to that of Warren et al. [59] for instance, does not affect the large scale matter predictions, and changes the results in the non-linear regime by a few percent. Note that for the bispectrum, as was shown by [46], a more important issue to be aware of is the finite volume effect, which can change the halo model predictions significantly for small volumes. The halo bias factors associated with this mass function are reported in [46]; we use these in what follows. [36] describe other empirical approaches to determining halo bias parameters.

B. Density profiles in redshift space

Consider the 6-D phase space density distribution function for dark matter particles within a particular halo, denoted $\mathcal{F}(\mathbf{x},\mathbf{u}|M)$. The density profile and velocity distribution function may be obtained by marginalizing over velocities and positions, respectively:

$$\rho(\mathbf{x}) = M\int d\mathbf{u}\,\mathcal{F}(\mathbf{x},\mathbf{u}|M)\,;\ \ \mathcal{V}_{3\rm D}(\mathbf{u}) = \int d\mathbf{x}\,\mathcal{F}(\mathbf{x},\mathbf{u}|M), \quad (12)$$

where M is the normalizing mass. The redshift space density profile can be readily obtained from the phase space distribution through transformation to the new random variable $\mathbf{s}$, given by our fundamental mapping (Eq. 3). Hence

$$\begin{aligned}\rho^s(\mathbf{s}_\perp,s_z) &= M\int dz\,d\mathbf{x}_\perp\,du_z\,d\mathbf{u}_\perp\,\mathcal{F}(\mathbf{x}_\perp,z,\mathbf{u}_\perp,u_z|M)\\ &\quad\times\delta^D(s_z-z+u_z)\,\delta^D(\mathbf{s}_\perp-\mathbf{x}_\perp),\\ &= M\int dz\,d\mathbf{u}_\perp\,\mathcal{F}(\mathbf{s}_\perp,z,\mathbf{u}_\perp,z-s_z|M)\ . \quad (13)\end{aligned}$$

We now assume that, in the absence of continued merging and accretion, each halo will dynamically relax under gravity, so particle orbits will isotropize and a spherically symmetric structure will be generated. Furthermore, we will assume that in this state of dynamical quasi-equilibrium, particle velocities will be independent of position within the halo. Thus, the phase space will be separable, i.e. $\mathcal{F}(\mathbf{x},\mathbf{u}|M) = \rho(\mathbf{x}|M)\mathcal{V}_{3\rm D}(\mathbf{u}|M)/M$. Since the velocity distribution function is isotropic it may now be written as the product of three independent distributions in the three coordinate directions: $\mathcal{V}_{3\rm D}(\mathbf{u}|M) = \mathcal{V}_{1\rm D}(u_x|M)\mathcal{V}_{1\rm D}(u_y|M)\mathcal{V}_{1\rm D}(u_z|M)$; and we shall hereafter use the notation that $\mathcal{V}_{1\rm D}\equiv\mathcal{V}$. Hence,

$$\rho^s(\mathbf{s}_\perp,s_z|M) = \int dz\,\rho(\mathbf{x}_\perp,z|M)\,\mathcal{V}(s_z-z|M). \quad (14)$$

Fourier transforming yields the compact expression

$$U^s(\mathbf{k}_\perp, k_z|M) = U(k|M)\,\mathcal{V}(\mu k|M)\ , \qquad (15)$$

where $\mathbf{k}_\perp$ denotes a 2-D wavevector perpendicular to the distortion, and $k_z = \mu k = \mathbf{k}\cdot\hat{\mathbf{z}}$ is parallel to it.

This expression shows that the redshift space profile is anisotropic because the spherically symmetric real-space profile U has been convolved along the line-of-sight direction with displacements generated by the velocity distribution $\mathcal{V}$. That is to say, $\mathcal{V}$ is the quantity in the model which generate FOG distortions and since it represents virial motions, it is clearly the sort of nonlinear effect that PTs based approaches must model 'ad hoc'. We also note that if $\mathcal{V}$ makes the redshift profile substantially anisotropic, then these nonlinear effects may extend farther into the linear regime than one might otherwise have expected.

We caution that this simple model of the halo phase space will almost certainly not be valid on a case by case basis[93]. However, if one considers the ensemble average of the phase space distribution of each halo, then this model corresponds closely to that found in simulations [41]. Precise details of the models we employ for the density profile of dark matter and for the 1-Point distribution function of velocities are presented in Appendix B. Note also that owing to these models employing different conventions for the halo mass we must convert between them, and we do this using our procedure from [65] and see Appendix B 2 for some details.

C. Halo center clustering in redshift space

On large scales the success of our analytic model will primarily be determined by its ability to reproduce the large-scale clustering of the halo centers. For this we use the redshift space Halo-PT developed in [42], which is accurate up to the 1-loop level in perturbation theory. The main result we draw from that work is the idea that the halo density field may be written as perturbation series that involves the standard density PT kernels [6] and the non-linear bias parameters [7]. Explicitly we have the series,

$$\delta^s_{\rm hc}(\mathbf{k}, a|M, R) = \sum_{n=0}^{\infty}[D_1(a)]^n[\delta^s_{\rm hc}(\mathbf{k}|M,R)]_n \qquad (16)$$

$$[\delta^s_{\rm hc}(\mathbf{k}|M,R)]_n = \int\prod_{i=1}^{n}\left\{\frac{d^3q_i}{(2\pi)^3}\,\delta_1(\mathbf{q}_i)\right\}(2\pi)^3\left[\delta^D(\mathbf{k})\right]_n \times Z^{\rm hc}_n(\mathbf{q}_1,...,\mathbf{q}_n|M,R), \qquad (17)$$

where $D(t)$ is the linear theory growth function and $f(\Omega)\equiv d\log D(a)/d\log a$ is the logarithmic growth rate of the velocity field. The functions $Z^{\rm hc}_n(\mathbf{q}_1,...,\mathbf{q}_n|M,R)$ are the redshift space Halo-PT kernels symmetrized in all of their arguments and we make explicit their dependencies on halo mass and the scale over which the density field has been smoothed. Kernels up to second order are [33, 35, 66]:

$$Z^{\rm hc}_0 = F^{\rm hc}_0 \equiv b_0\ ; \qquad (18)$$

$$Z^{\rm hc}_1 = F^{\rm hc}_1 + f(\Omega)\mu^2_{q_1}\tilde{G}_1\,[1+b_0]\ ; \qquad (19)$$

$$Z^{\rm hc}_{1,2} = F^{\rm hc}_{1,2} + f(\Omega)\mu^2_k\tilde{G}_{1,2} + \frac{1}{2}f(\Omega)\mu_k k\left\{\frac{\mu_{q_1}}{q_1}\tilde{G}_1\left[F^{\rm hc}_2 + f(\Omega)\mu^2_{q_2}\tilde{G}_2\right] + \frac{\mu_{q_2}}{q_2}\tilde{G}_2\left[F^{\rm hc}_1 + f(\Omega)\mu^2_{q_1}\tilde{G}_1\right]\right\} + \frac{1}{2}\left[f(\Omega)\mu_k k\right]^2\frac{\mu_{q_1}}{q_1}\frac{\mu_{q_2}}{q_2}\tilde{G}_1\tilde{G}_2\,b_0\ , \qquad (20)$$

where we have written the direction cosines of k-vectors along the z-axis as

$$\mu = \hat{\mathbf{k}}\cdot\hat{\mathbf{z}}\ ; \qquad \mu_{i_1\ldots i_n} \equiv \frac{(\mathbf{q}_{i_1}+\cdots+\mathbf{q}_{i_n})\cdot\hat{\mathbf{z}}}{|\mathbf{q}_{i_1}+\cdots+\mathbf{q}_{i_n}|}\ . \qquad (21)$$

We have also adopted the short-hand notation:

$$Z^{\rm hc}_{i_1,\ldots,i_n} \equiv Z^{\rm hc}_n(\mathbf{q}_{i_1},\ldots,\mathbf{q}_{i_n}|M,R)\ ;$$
$$F^{\rm hc}_{i_1,\ldots,i_n} \equiv F^{\rm hc}_n(\mathbf{q}_{i_1},\ldots,\mathbf{q}_{i_n}|M,R)\ ;$$
$$\tilde{G}_{i_1,\ldots,i_n} \equiv W(|\mathbf{q}_{i_1}+\cdots+\mathbf{q}_{i_n}|\,R)G_n(\mathbf{q}_{i_1},\ldots,\mathbf{q}_{i_n})\ . \qquad (22)$$

The quantities $F^{\rm hc}_n$ are the nth order Halo-PT kernels (see Appendix C and [36] for complete details). The functions G_n represent the nth order Eulerian PT kernels for the divergence of the velocity field [6]. Note that these expressions are almost identical to the redshift space PT kernels derived by [35] and separately by [33], however they differ in some subtle ways: one, we have explicitly included their dependence on the smoothing filter, which is needed to facilitate the Taylor expansion; and two, we are applying this in the context of haloes and not galaxies and so they depend on the non-linear halo bias parameters $b_i(M)$ (see discussion in Section III A). Note that we have also included $b_0(M)$, since this does not have to be zero, although we will take it to be so for all our later analysis.

Following standard methods for calculating polyspectra, we find that the halo center bispectrum, $B^s_{\rm hc,123}\equiv B^s_{\rm hc}(\mathbf{k}_1,\mathbf{k}_2,\mathbf{k}_3|M_1,M_2,M_3,R)$, up to fourth order in redshift space Halo-PT, is

$$B^s_{\rm hc,123} = 2P_{11}(k_1)P_{11}(k_2)\,Z^{\rm hc}_1(\mathbf{k}_1|M_1,R)\,Z^{\rm hc}_1(\mathbf{k}_2|M_2,R) \times Z^{\rm hc}_2(\mathbf{k}_1,\mathbf{k}_2|M_3,R) + {\rm cyc\ 2}\ . \qquad (23)$$

Inserting our expressions for the redshift space Halo-PT kernels, Eqs (18–20), in to the above expression, reveals:

$$\frac{B^s_{\rm hc,123}(M_1,M_2,M_3)}{W(k_1R)W(k_2R)W(k_3R)} = 2b_1(M_1)b_1(M_2)b_1(M_3)P_{11}(k_1)P_{11}(k_2)\prod_{i=1,2}\left\{1+\beta_i\,\mu_i^2\left[1+b_0(M_i)\right]\right\}$$
$$\times\left[F_2(\mathbf{k}_1,\mathbf{k}_2)+\beta_3\,\mu_3^2 G_2(\mathbf{k}_1,\mathbf{k}_2)+\frac{W(k_1R)W(k_2R)}{W(k_3R)}\left(\frac{c_2(M_3)}{2}+\frac{1}{2}\left[f(\Omega)\mu_{k_3}k_3\right]^2\frac{\mu_{k_1}}{k_1}\frac{\mu_{k_2}}{k_2}c_0(M_3)\right.\right.$$
$$\left.\left.+\frac{1}{2}f(\Omega)\mu_{k_3}k_3\left\{\frac{\mu_{k_1}}{k_1}\left[1+\beta_3\,\mu_{k_2}^2\right]+\frac{\mu_{k_2}}{k_2}\left[1+\beta_3\,\mu_{k_1}^2\right]\right\}\right)\right]+2\,\text{cyc.} \quad (24)$$

where $\beta_i \equiv f(\Omega)/b_1(M_i)$ and where $c_j(M_i) = b_j(M_i)/b_1(M_i)$. As in our real space work on the power spectrum, we are now faced with the situation that we have solved for the bispectrum of halo centers filtered on scale R, and in fact we would like to recover the unfiltered bispectrum. As in [36], we take the following *ansatz*: the filtering of the spectra can be reversed through the following operation:

$$P(\mathbf{k}) \equiv \frac{P(\mathbf{k}|R)}{W^2(kR)}\,;$$
$$B(\mathbf{k}_1,\mathbf{k}_2,\mathbf{k}_3) \equiv \frac{B(\mathbf{k}_1,\mathbf{k}_2,\mathbf{k}_3|R)}{W(k_1R)W(k_2R)W(k_3R)} \quad (25)$$

and this explains the form of the left-hand-side of Eq. (24). An alternative approach to the filtering issue for the power spectrum and bispectrum was proposed by [67], and we shall leave the solution of this problem as an open issue for future consideration.

With these ingredients prepared, we are now in full possession of a complete description of the bispectrum of galaxies haloes and dark matter in the halo model and in the presence of a local, non-linear scale dependent bias. In the next section we develop these equations further.

IV. THE ISOTROPIC BISPECTRUM

A. Euler angle averages

The redshift space bispectrum is an anisotropic function on the sphere that depends on 5 variables. The first three are the triangle configuration, and the other two specify its orientation with respect to the z-axis. However it is common practice to measure this quantity averaged over all possible orientations of the coordinate frame. Thus to compare with this isotropized observable, we shall now derive the isotropized form for the halo model, which we shall denote $\hat{B}^s$. Interestingly, the following approach is identical to that which one performs for the triaxial halo model in real space [19, 65], since on small scales, one may effectively think of transforming to redshift space as simply transforming a set of spherical haloes into a set of prolate ellipsoids whose semi-major axes all point along the line-of-sight. Of course, the real situation is more complex, since the halo centers are also distorted according to the halo velocity projected along the line-of-sight, but nevertheless we may borrow some mathematical machinery from the triaxial halo analysis.

The isotropic function is thus,

$$\hat{B}^s(k_1,k_2,\theta_{12}) = \frac{1}{8\pi^2}\int d\gamma_1\, d(\cos\gamma_2)\, d\gamma_3 \times B^s\left[\mathcal{R}(\gamma_1,\gamma_2,\gamma_3)\mathbf{k}_1,\mathcal{R}(\gamma_1,\gamma_2,\gamma_3)\mathbf{k}_2\right], \quad (26)$$

where $\mathcal{R}(\gamma_1,\gamma_2,\gamma_3)$ is the rotation matrix for the components of the basis vectors. $\mathcal{R}(\gamma_1,\gamma_2,\gamma_3)$ is parametrized by three position or Euler angles, (γ_1,γ_2,γ_3) and these are the $z'-y'-z''$ rotation angles (see Appendix D for the explicit form of the matrix we use). Note that we assign uniform probability on the sphere to each triple of angles.

The following considerations simplify this expression considerably. Firstly, in the PT expressions for B^s, each term depends on either the angle between two k-vectors or the projection of each vector along the z-axis. In the first case, the use of matrix notation shows that

$$\left[\mathbf{k}_i'\right]^T\mathbf{k}_j' = \left[\mathcal{R}(\gamma_1,\gamma_2,\gamma_3)\mathbf{k}_i\right]^T\mathcal{R}(\gamma_1,\gamma_2,\gamma_3)\mathbf{k}_j$$
$$= \mathbf{k}_i^T\mathcal{R}(\gamma_1,\gamma_2,\gamma_3)^T\mathcal{R}(\gamma_1,\gamma_2,\gamma_3)\mathbf{k}_j$$
$$= \mathbf{k}_i^T\mathbf{k}_j\,; \quad (27)$$

this is the well-known result that scalar products are invariant under rotations of the coordinate basis functions. In the second case, the projection of each rotated vector onto the line of sight direction (or z-axis) can be written

$$\mathbf{k}'\cdot\hat{\mathbf{z}} = \mathcal{R}(\gamma_1,\gamma_2,\gamma_3)\mathbf{k}\cdot\hat{\mathbf{z}}$$
$$= k_x\sin\gamma_2\,\cos\gamma_1 + k_y\sin\gamma_2\,\sin\gamma_1 + k_z\cos\gamma_2$$
$$\equiv A(\mathbf{k},\gamma_1,\gamma_2)\,, \quad (28)$$

Thus, we see that the resultant function must be invariant under the γ_3 rotation, and hence this integral may be computed trivially. Finally, because our final quantity $\hat{B}$ must be independent of the initial locations of the k-vector triple, we may without loss of generality choose these locations to be as convenient as possible. Therefore, we let the initial $\mathbf{k}_1$ vector lie along the polar-axis and constrain $\mathbf{k}_2$ and $\mathbf{k}_3$ to lie in the z–y plane: i.e.

$$\left[\mathbf{k}_1\right]^T = (0,\,0,\,k_1)$$
$$\left[\mathbf{k}_2\right]^T = (0,\,k_2\cos\theta_{12},\,k_2\sin\theta_{12})$$
$$\left[\mathbf{k}_3\right]^T = (0,\,-k_2\cos\theta_{12},\,-k_1-k_2\sin\theta_{12}) \quad (29)$$

where the last equality uses the closure condition: $\sum_i \mathbf{k}_i = 0$. Thus, the k-vectors rotated into the new basis and dotted with the z-direction are now written:

$$\begin{aligned} A_1 &= \cos\gamma_2\,(k_1)_z\ ; \\ A_2 &= \sin\gamma_2\ \sin\gamma_1\,(k_2)_y + \cos\gamma_2\,(k_2)_z\ ; \\ A_3 &= -\sin\gamma_2\ \sin\gamma_1\,(k_2)_y - \cos\gamma_2\,[(k_1)_z + (k_2)_z]\ . \end{aligned} \quad (30)$$

The parameters $A_i \equiv A(\mathbf{k}_i, \gamma_1, \gamma_2)$ are simply related to the cosines of the k-vectors along the z-axis:

$$\mu_1 = \frac{A_1}{k_1}\ ;\quad \mu_2 = \frac{A_2}{k_2}\ ;\quad \mu_3 = -\frac{q\mu_2 + \mu_1}{[1 + q^2 + 2q\cos(\theta_{12})]^{1/2}}\ , \quad (31)$$

where $q \equiv k_2/k_1$.

We may now apply the above operation directly to our expressions for the anisotropic bispectrum (Eqs 9–11). On inserting the A_i into each instance of μ_i in the density profiles (Eq. 15) and the halo center power spectra and bispectrum (Eqs E4 & 24), we find that the 1-, 2- and 3-Halo terms for the isotropic bispectrum become

$$\hat{B}^s_{1\rm H}(k_1,k_2,\theta_{12}) = \frac{1}{4\pi\bar{\rho}^3_\alpha}\int d\gamma_1\, d(\cos\gamma_2)\int dM\,[W_\alpha]^3\,n(M)\prod_{i=1}^{3}\{U(k_i|M)\mathcal{V}(\mu_i k_i|M)\}\ ; \quad (32)$$

$$\begin{aligned}\hat{B}^s_{2\rm H}(k_1,k_2,\theta_{12}) &= \frac{1}{4\pi\bar{\rho}^3_\alpha}\int d\gamma_1\, d(\cos\gamma_2)\prod_{i=\{1,2\}}\left\{\int dM_i\,[W_\alpha]_i\,b_1(M_i)n(M_i)\,U(k_i|M_i)\mathcal{V}(\mu_i k_i|M_i)\right\} \\ &\times[W_\alpha]_1\,U(k_3|M_1)\,\mathcal{V}(\mu_3 k_3|M_1)P_{11}(k_2)\left\{\,1 + [\beta_1+\beta_2]\,\mu_2^2 + \beta_1\,\beta_2\mu_2^4\right\} + \text{cyc}\ ; \end{aligned} \quad (33)$$

$$\begin{aligned}\hat{B}^s_{3\rm H}(k_1,k_2,\theta_{12}) &= \frac{1}{4\pi\bar{\rho}^3_\alpha}\int d\gamma_1\, d(\cos\gamma_2)\prod_{i=1}^{3}\left\{\int dM_i\,[W_\alpha]_i\,n(M_i)\,U(k_i|M_i)\,\mathcal{V}(\mu_i k_i|M_i)\right\} \\ &\times B^s_{\rm hc}(k_1,k_2,\theta_{12},\mu_1,\mu_2|M_1,M_2,M_3)\ . \end{aligned} \quad (34)$$

The only variables that depend on the Euler angles γ_1 and γ_2 are μ_i and A_i. Each term requires evaluation of no more than a 4-D embedded integral: two integrals for the Euler angles, one for the mass, and one for the Fourier transform of the density profile. Note that for simplicity, we have kept only the leading order contribution to the the 2-Halo term. Technically this should be taken up to the 1-Loop level to be consistent with the bispectrum which is 4th order in δ. However, this issue is beyond the scope of the current paper and will be addressed in [42].

B. Computational considerations

Our expressions for the bispectrum as presented above are complete. However some calculational effort is still required before we may attempt a practical implementation on the computer. We now present some simplifications.

We begin by defining some convenient notation: Let $\psi^{(i)}_{\delta,j}$ and $\psi_{v,j}$ denote the following integrals:

$$\begin{aligned}\psi^{(i)}_{\delta,j}(\mathbf{k}_1,\ldots,\mathbf{k}_j) &= \frac{1}{\bar{\rho}^j_\alpha}\int dM\,n(M)\,b_i(M) \\ &\times\prod_{l=1}^{j}\left\{\,[W_\alpha]U(k_l|M)\mathcal{V}(\mu_l k_l|M)\right\}\ ; \end{aligned} \quad (35)$$

$$\begin{aligned}\psi_{v,j}(\mathbf{k}_1,\ldots,\mathbf{k}_j) &= \frac{f(\Omega)}{\bar{\rho}^j_\alpha}\int dM\,n(M) \\ &\times\prod_{l=1}^{j}\left\{\,[W_\alpha]U(k_l|M)\mathcal{V}(\mu_l k_l|M)\right\}\ . \end{aligned} \quad (36)$$

The first integral generalizes the halo bias weighting scheme applied to the density field for the situation where j-points are within a single halo. The second integral generalizes the weighting scheme to the similar situation for the halo velocity field. This notation has some similarities with that of [40], but is different in the way in which the velocity field is treated – recall that the velocity field has been assumed to be unbiased.

In this notation we may re-write the 2- and 3-Halo terms in the bispectrum; the 1-Halo term requires no simplification. Through rearrangement of the mass integrals and expansion of the halo center power spectrum through substitution of the appropriate kernels, we find that the 2-Halo term can now be written

$$\hat{B}^s_{\alpha,2\rm H}(k_1,k_2,\theta_{12}) \;=\; \frac{1}{4\pi}\int d\gamma_1\, d(\cos\gamma_2)\,\Big\{P(k_2)\Big[\psi^{(1)}_{\delta,2}(\mathbf{k}'_1,\mathbf{k}'_3)\psi^{(1)}_{\delta,1}(\mathbf{k}'_2) + \Big(\psi_{v,2}(\mathbf{k}'_1,\mathbf{k}'_3)\psi^{(1)}_{\delta,1}(\mathbf{k}'_2)+\psi^{(1)}_{\delta,2}(\mathbf{k}'_1,\mathbf{k}'_3)\psi_{v,1}(\mathbf{k}'_2)\Big)\,\mu_2^2 + \psi_{v,2}(\mathbf{k}'_1,\mathbf{k}'_3)\psi_{v,1}(\mathbf{k}'_2)\,\mu_2^4\Big] + 2\,\mathrm{cyc}\Big\}\;. \tag{37}$$

The 3-Halo term is significantly more complex, owing to the halo center bispectrum being the product of two first order kernels and one second order kernel. Nevertheless, we may again isolate the integrals over mass and use the ψ functions to obtain

$$\hat{B}^s_{3\rm H}(k_1,k_2,\theta_{12}) \;=\; \frac{1}{4\pi}\int d\gamma_1\, d(\cos\gamma_2)\,\Big\{\,2P(k_1)P(k_2)T_1(\mathbf{k}'_1,\mathbf{k}'_2) \times\left[T_2(\mathbf{k}'_1,\mathbf{k}'_2|\mathbf{k}'_3)\psi^{(1)}_{\delta,1}(\mathbf{k}'_3)+T_3(\mathbf{k}'_1,\mathbf{k}'_2|\mathbf{k}'_3)\psi_{v,1}(\mathbf{k}'_3)+\mathcal{W}_{12,3}\frac{\psi^{(2)}_{\delta,1}(\mathbf{k}'_3)}{2}+T_4(\mathbf{k}'_1,\mathbf{k}'_2|\mathbf{k}'_3)\psi^{(0)}_{\delta,1}(\mathbf{k}'_3)\right]+2\,\mathrm{cyc}\Big\}\;; \tag{38}$$

where we have defined the following useful quantities:

$$T_1(\mathbf{k}_i,\mathbf{k}_j) \;=\; \prod_{m=i,j}\Big\{\psi^{(1)}_{\delta,1}(\mathbf{k}_m)+\mu_m^2\Big[\psi_{v,1}(\mathbf{k}_m)+f(\Omega)\psi^{(0)}_{\delta,1}(\mathbf{k}_m)\Big]\Big\}\;; \tag{39}$$

$$T_2(\mathbf{k}_i,\mathbf{k}_j|\mathbf{k}_l) \;=\; F_2(\mathbf{k}_i,\mathbf{k}_j)+\frac{1}{2}\mathcal{W}_{ij,l}f(\Omega)\mu_l k_l\left[\frac{\mu_i}{k_i}+\frac{\mu_j}{k_j}\right]\;; \tag{40}$$

$$T_3(\mathbf{k}_i,\mathbf{k}_j|\mathbf{k}_l) \;=\; \mu_l^2 G_2(\mathbf{k}_i,\mathbf{k}_j)+\frac{1}{2}\mathcal{W}_{ij,l}f(\Omega)\mu_l k_l\left[\frac{\mu_i}{k_i}\mu_j^2+\frac{\mu_j}{k_j}\mu_i^2\right]\;; \tag{41}$$

$$T_4(\mathbf{k}_i,\mathbf{k}_j|\mathbf{k}_l) \;=\; \frac{1}{2}\mathcal{W}_{ij,l}\left[f(\Omega)\mu_l k_l\right]^2\frac{\mu_i}{k_i}\frac{\mu_j}{k_j}\;; \tag{42}$$

and

$$\mathcal{W}_{ij,l}\equiv\frac{W(k_iR)W(k_jR)}{W(k_lR)}\;. \tag{43}$$

The advantage of this reformulation of the 2– and 3–Halo terms is that we have decomposed the integrand into a set of algebraic functions of the ψ integrals (Eqs 35–36), and auxiliary functions, and these may all be computed in parallel making the computation highly modular.

C. The large scale limit

Next we consider the redshift space bispectrum in the very large scale limit, as this should asymptotically reduce to the standard PT expressions for the bispectrum, modulo discreteness corrections for the point process associated with the halo field. However, let us first examine the large scale limit of Eqs (35) and (36). On letting $\{\mathbf{k}_i\}\to 0$, the density profile terms become $U^s(\mathbf{k}_i)\to 1$, the window function becomes $\mathcal{W}_{ij,l}\to 1$, and so

$$\lim_{\{k_j\}\to 0}\psi^{(i)}_{\delta,j}=\frac{\langle b_i(M)[W_\alpha]^j\rangle}{\langle[W_\alpha]\rangle^j}\;;$$
$$\lim_{\{k_j\}\to 0}\psi_{v,j}=\frac{f(\Omega)\,\langle[W_\alpha]^j\rangle}{\langle[W_\alpha]\rangle^j}\;; \tag{44}$$

where $\langle\ldots\rangle=\int dMp(M)\ldots$, with $p(M)\equiv n(M)/\bar{n}_{\rm H}$, $\bar{n}_{\rm H}$ being the total number density of haloes in the required mass range. When $j=1$ we write these functions more simply as: the average non-linear bias parameter for the tracer particles, $\psi^{(i)}_{\delta,1}\equiv\overline{b}_{\alpha,i}$, and the logarithmic growth factor for the linear velocity field $\psi_{v,1}\equiv f(\Omega)$.

The bispectrum in the large-scale limit can now be

computed directly. The 1-Halo term is trivially obtained, and the 2- and 3-Halo terms can be developed through replacing the ψ functions in the general expressions (37) and (38), for their large scale forms (44). After some algebraic manipulation we arrive at the result

$$\hat{B}^s_\alpha(k_1,k_2,\theta_{12}) \;=\; \hat{B}^s_{\alpha,\rm PT}(k_1,k_2,\theta_{12}) + \frac{1}{\bar{n}_{\alpha,\rm 2H}}\left[P(k_2)+P(k_3)+P(k_1)\right] + \frac{1}{\bar{n}^2_{\alpha,\rm 1H}} \;; \quad (45)$$

where the large scale isotropic PT bispectrum in redshift space is given by

$$\hat{B}^s_{\alpha,\rm PT}(k_1,k_2,\theta_{12}) \;=\; \frac{1}{4\pi}\int d\gamma_1\, d(\cos\gamma_2) \prod_{i=1,2}\left\{\overline{b}_{\alpha,1}+\mu_i^2 f(\Omega)\left[1+\overline{b}_{\alpha,0}\right]\right\} \times \left\{2P(k_1)P(k_2)\left[\overline{b}_{\alpha,1}T_2(\mathbf{k}_1,\mathbf{k}_2|\mathbf{k}_3)+f(\Omega)T_3(\mathbf{k}_1,\mathbf{k}_2|\mathbf{k}_3)+\frac{\overline{b}_{\alpha,2}}{2}+\overline{b}_{\alpha,0}\,T_4(\mathbf{k}_1,\mathbf{k}_2|\mathbf{k}_3)\right]\right\} + 2 \text{ cyc} \quad (46)$$

this is equivalent to that found by [33]. We also defined the 1– and 2–Halo *'effective'* number densities to be:

$$\frac{1}{\bar{n}^2_{\alpha,\rm 1H}} \;=\; \frac{\langle W^3_\alpha\rangle}{\langle W_\alpha\rangle^3} \;; \quad (47)$$

$$\frac{1}{\bar{n}_{\alpha,\rm 2H}} \;=\; \frac{\langle b_1(M)[W_\alpha]^2\rangle}{\langle W_\alpha\rangle^2}\overline{b}_{\alpha,1} + \frac{f(\Omega)^2}{5}\frac{\langle [W_\alpha]^2\rangle}{\langle W_\alpha\rangle^3} + \frac{f(\Omega)}{3}\left[\frac{\langle [W_\alpha]^2\rangle}{\langle W_\alpha\rangle^2}\overline{b}_{\alpha,1} + \frac{\langle b_1(M)[W_\alpha]^2\rangle}{\langle W_\alpha\rangle^3}\right] \quad (48)$$

Our final expression for the large scale limit (Eq. 45) is similar to the standard theoretical expectation for the bispectrum recovered from a Poisson point process sampling of a continuous field (c.f. Section 43. [68]). However, the effective shot-noise terms (the last two terms on the right hand side of Eq. 45), are very different from the standard form, which would simply have e.g. $\bar{n}_{\alpha,\rm 2H} = \bar{n}_\alpha$. These effective number densities, Eqs (47) and (48), represent the fact that in the halo model we assume that dark matter haloes are Poisson sampled into the density field and that the tracer particles are injected into these haloes, and so simply act as different weights. The issue of sampling tracer particles into the density field has very strong implications for how one should extract information from galaxy surveys. We shall reserve this investigation for future work. Before continuing though, we note that these expressions are the halo model 'effective shot noise' terms for the redshift space halo model.

Finally, we also note that on setting $f(\Omega) = 0$, one may recover the 1-Loop PT bispectrum in real space for a set of biased tracer particles α.

D. The small-scale limit and hierarchical models

On small scales, the bispectrum is dominated by the 1-Halo term, given by Eq. (32). Our understanding of its behavior in this limit can be guided by considering the case where all haloes are of the same mass. In this situation we have that $n(M) \to \delta^D(M-M')\bar{n}_{\rm H}$ and $\bar{\rho}_\alpha \to \bar{n}_{\rm H}[W_\alpha]$. Applying these conditions to our expression Eq. (32), we have:

$$\hat{B}^s_{\rm 1H}(k_1,k_2,\theta_{12}|M) \;=\; \frac{1}{4\pi\bar{n}^2_{\rm H}}\int d\gamma_1\, d(\cos\gamma_2) \times \prod_{i=1}^{3}\left\{U(k_i|M)\mathcal{V}(\mu_i k_i|M)\right\} \;. \quad (49)$$

We may follow this same procedure for the power spectrum (see Eq. E2) and so construct the reduced bispectrum, whence

$$Q_s = \frac{\int d\gamma_1\, d(\cos\gamma_2)\prod_{i=1}^3\left\{\mathcal{V}(\mu_i k_i|M)/U(k_i|M)\right\}/4\pi}{\mathcal{R}^{(0)}_{1,2}(a_1)\mathcal{R}^{(0)}_{1,2}(a_2)/U(k_3|M)^2 + 2\text{cyc}} \quad (50)$$

where $\mathcal{R}^{(0)}_{1,2}(a_1)$ is given by Eq. (E9). Notice that this expression no longer depends on the weights $[W_\alpha]$ or number densities of tracers $\bar{n}_{\rm H}$, but simply the real space profile and the 1-PT velocity profile. If the density and velocity profiles were mass independent, then Eq. (50) would be a constant and hence hierarchical for all haloes. However, for realistic redshift space profiles, this is not the case (see Appendix B). Thus if the halo model were a good description for small scale clustering, then the hierarchical model is unlikely to be correct in real or redshift space, and we may generally extend this statement to any tracers of the density field. Finally, and somewhat interestingly, notice that if the ratio $\mathcal{V}(\mu_i k_i|M)/U(k_i|M)$ is mass independent, then the configuration dependence of

the bispectrum becomes universal, modulo an amplitude off-set.

E. The White-Seljak Approximation

The White-Seljak approximation (hereafter WS) is the supposition that we may perform the orientation average separately for each halo and the large scale halo clustering terms [39, 40]. In the triaxial halo model, [65] showed that the overall contribution from halo alignment to the matter power spectrum was negligible. Thus we may similarly assume that on large-scales the 2– and 3–Halo terms will not be sensitive to the orientation of the FOGs – and this allows us to use the isotropic redshift space density profiles instead of the anisotropic profiles. However, since the bispectrum is more sensitive than the power spectrum to the shapes of structure, we shall be a little more cautious, and demonstrate the validity of this approximation.

In the WS approximation we therefore take,

$$\hat{\psi}^{(i)}_{\delta,1}(k_1) \equiv \frac{1}{4\pi}\int d\gamma_1\, d(\cos\gamma_2)\, \psi^{(i)}_{\delta,1}(\mathbf{k}'_1)\ ,$$
$$\hat{\psi}^{(i)}_{\delta,1}(k_1,k_2,\theta_{12}) \equiv \frac{1}{4\pi}\int d\gamma_1\, d(\cos\gamma_2)\, \psi^{(i)}_{\delta,2}(\mathbf{k}'_1,\mathbf{k}'_2)\ , \quad (51)$$

and with similar expressions for the $\hat{\psi}_{v,j}$ functions. On replacement of these terms into Eq. (37) we find that the 2-Halo term simplifies to:

$$\begin{aligned}\hat{B}^{s,\mathrm{WS}}_{\alpha,2\mathrm{H}}(k_1,k_2,\theta_{12}) \;=\; & P(k_2)\Big\{\,\hat{\psi}^{(1)}_{\delta,2}(k_1,k_3,\theta_{13})\hat{\psi}^{(1)}_{\delta,1}(k_2)\\ & +\frac{1}{3}\Big[\hat{\psi}_{v,2}(k_1,k_3,\theta_{13})\hat{\psi}^{(1)}_{\delta,1}(k_2)\\ & +\,\hat{\psi}^{(1)}_{\delta,2}(k_1,k_3,\theta_{13})\hat{\psi}_{v,1}(k_2)\Big]\\ & +\,\frac{1}{5}\hat{\psi}_{v,2}(k_1,k_3,\theta_{13})\hat{\psi}_{v,1}(k_2)\,\Big\} + 2\,\mathrm{cyc}\ . \quad (52)\end{aligned}$$

Similarly, on applying this approximation to Eq. (38), the 3-Halo term reduces to:

$$\begin{aligned}\hat{B}^{s,\mathrm{WS}}_{\alpha,3\mathrm{H}}(k_1,k_2,\theta_{12}) \;=\; & 2P(k_1)P(k_2)\int\frac{d\gamma_1}{4\pi}\,d(\cos\gamma_2)\\ & \times\hat{T}_1(\mathbf{k}'_1,\mathbf{k}'_2)\Big[\,T_2(\mathbf{k}'_1,\mathbf{k}'_2|\mathbf{k}'_3)\hat{\psi}^{(1)}_{\delta,1}(k_3)\\ & +T_3(\mathbf{k}'_1,\mathbf{k}'_2|\mathbf{k}'_3)\hat{\psi}_{v,1}(k_3)+\mathcal{W}_{12,3}\frac{\hat{\psi}^{(2)}_{\delta,1}(k_3)}{2}\\ & +\;T_4(\mathbf{k}'_1,\mathbf{k}'_2|\mathbf{k}'_3)\hat{\psi}^{(0)}_{\delta,1}(k_3)\Big] + 2\,\mathrm{cyc}\ ; \quad (53)\end{aligned}$$

where

$$\begin{aligned}\hat{T}_1(\mathbf{k}_i,\mathbf{k}_j) \;=\; & \prod_{m=i,j}\Big\{\hat{\psi}^{(1)}_{\delta,1}(k_m)+\mu_m^2\Big[\hat{\psi}_{v,1}(k_m)\\ & +\;f(\Omega)\hat{\psi}^{(0)}_{\delta,1}(k_m)\Big]\Big\}\ . \quad (54)\end{aligned}$$

This completes our analytic investigation. In the next sections we shall provide numerical evaluation of the bispectrum recovered from an exact evaluation in the WS approximation.

V. REDSHIFT SPACE BISPECTRUM RESULTS

A. Testing the WS approximation

Figure 1 compares the predictions for the configuration dependence of the reduced redshift space bispectrum for cluster mass haloes ($3.0\times10^{13}M_\odot\,h^{-1} < M < 5.0\times10^{15}M_\odot\,h^{-1}$) derived using the exact evaluation of Eqs (32,37,38) (thick/red lines) with the predictions generated under the WS approximation Eqs (32,52,53) (thin/blue lines). The top section of each panel shows the reduced bispectra for triangles with $k_2/k_1 = 2$ and for scales $k_1 = \{0.01, 0.1, 0.5, 1.0\}\,h\,\mathrm{Mpc}^{-1}$. The dash, dot-dash and dotted lines show the 1-, 2- and 3-Halo terms, respectively and the thick solid lines show their sum. The bottom section in each panel shows the ratio of the residuals of the exact evaluation with respect to the approximate results.

For very large scales, $k = 0.01h\,\mathrm{Mpc}^{-1}$, the approximation is almost perfect, $< 1\%$ deviations. This agrees entirely with our earlier derivation of the bispectrum in the large-scale limit, c.f. Eq. (45). This clearly shows that there is no dependence on the halo profiles and hence the WS approximation is reliable here. On intermediate scales $k_1 = \{0.1,\, 0.5\}h\,\mathrm{Mpc}^{-1}$ we find small departures between the evaluation of the exact expressions and the approximate ones of the order $< 7\%$. This is as expected – the approximation is less good where the 2- and 3-Halo terms are of the same order. We also note, that for a given scale, the largest deviations typically appear for the case of degenerate triangles, i.e. where the configuration of k-vectors are co-linear. This leads us to suppose that the equilateral bispectrum as a function of scale will show agreement at the level of $< 5\%$ under this approximation. Since current observational measurements of the bispectrum on large scales have sample and cosmic variance errors roughly of the order 50% on scales $k_1 \sim 0.1h\,\mathrm{Mpc}^{-1}$ and going down to a several percent at $k_1 \sim 1h\,\mathrm{Mpc}^{-1}$, we anticipate that, at least for the current data, this approximation should be sufficiently accurate. We highlight again that the main advantage of this approximation is the increased speed with which one can compute the bispectrum: the $\psi^{(i)}_{\delta,j}$ and $\psi_{v,j}$ functions are only evaluated once for a particular configuration, as opposed to thousands of times.

B. Comparison with other analytic models

Figure 2 shows the analytic predictions for the configuration dependence of the redshift space halo bispectrum

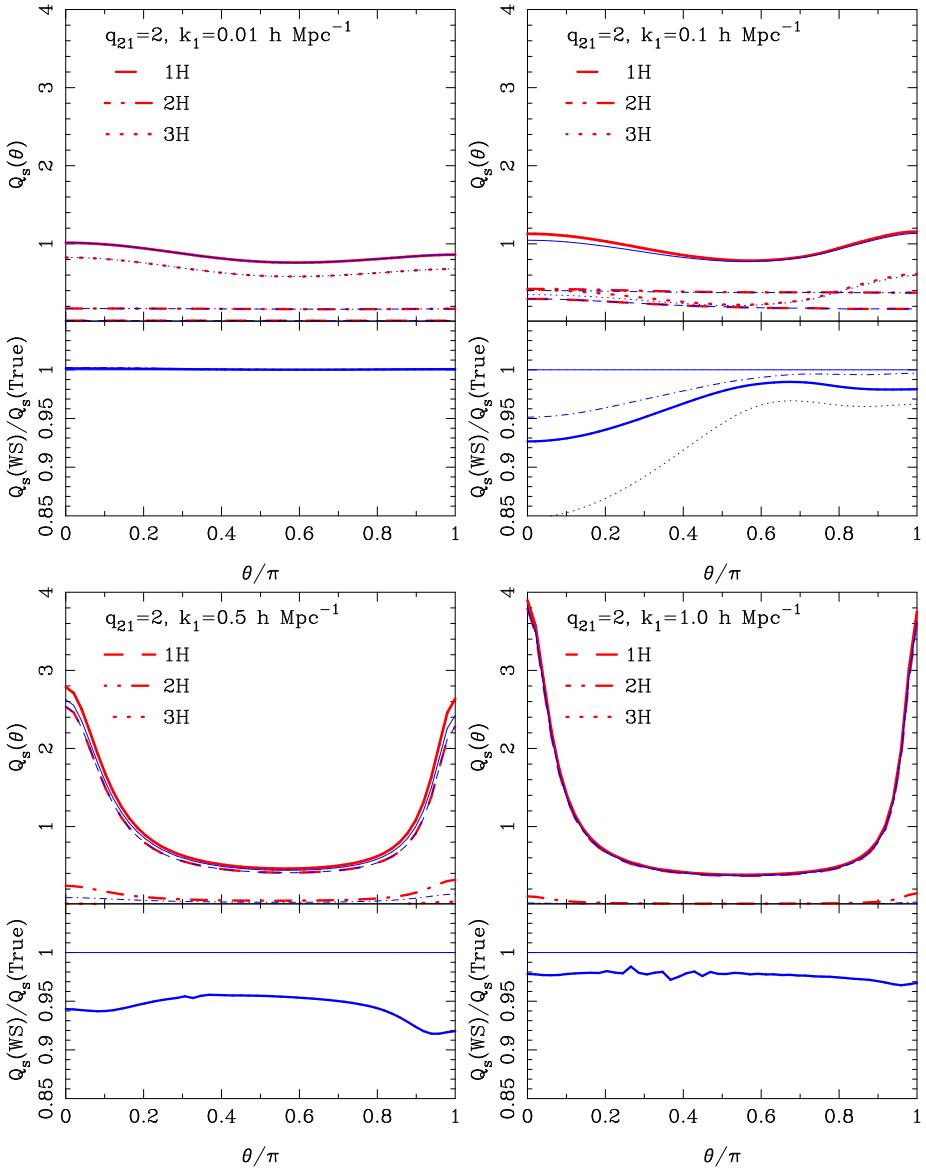

FIG. 1: (Top panels) Configuration dependence of the reduced bispectrum in redshift space, for mass weighted haloes in an LCDM cosmology – comparison of predictions from exact evaluation of the Halo Model with those from the WS-approximation. The top sections of show results for triangles with $k_2/k_1 = 2$ and for scales: $k_1 = \{0.01, 0.1, 0.5, 1.0\} h\,\mathrm{Mpc}^{-1}$. The dash, dot-dash and dotted lines in each panel correspond to the 1-, 2- and 3-Halo terms, respectively. The solid lines correspond to the sum. Thick (red) and thin (blue) lines are the exact and approximate results, respectively. (Bottom panels) Ratio of total WS approximate bispectra to exact calculation.

compared to several current analytic models in the literature. The four panels show again the triangles with k-vectors in the ratio 2:1 and for the same four scales as in the previous figure. The solid (red) lines in each panel show our HMs predictions in the WS approximation. The (red) dash lines show the PTs predictions with effective nonlinear bias parameters included [33]; explicitly this is our Eq. (46). The (blue) dotted line corresponds to the real space standard PT predictions, again with the effective nonlinear bias parameters included [6].

Considering the predictions on the largest scales $k_1 = 0.01\ h\,\mathrm{Mpc}^{-1}$ (top-left panel), we see that the HMs matches almost perfectly with the PTs result: a weak configuration dependence, indicating that on these very large scales non-linearity induces structures that are, on average, more filamentary than spherical [33, 75] (in this diagram spherical perturbations are best probed by isosceles triangles, $\theta_{12} \sim 2\pi/3$, since for the 2:1 triangles, this is the configuration closest to equilateral). However, we notice that there is a small deviation $< 5\%$ for the situation where the k_1 and k_2 vectors are parallel. This owes to the fact that the 1- and 2-Halo terms are non-vanishing as $k \to 0$, as discussed in Section IV C, and this gives rise to 'effective shot-noise' terms [68].

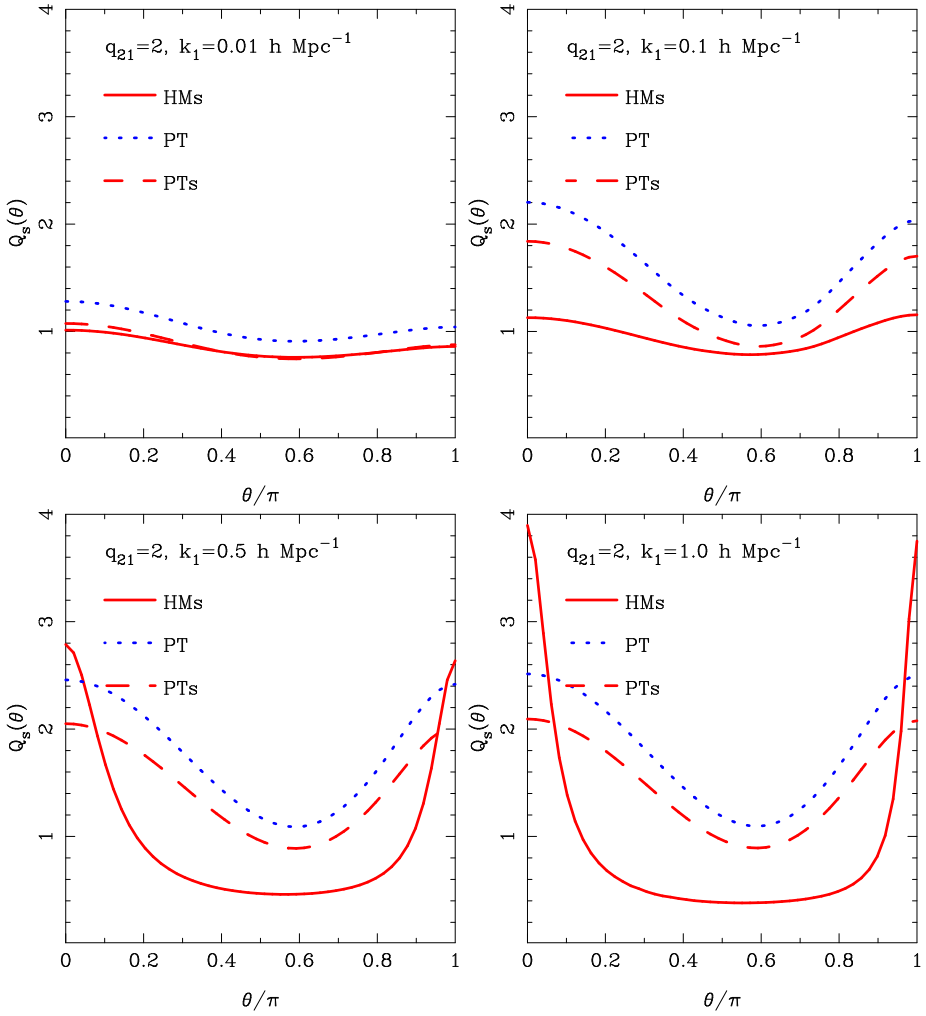

FIG. 2: Comparison of different analytic predictions for the configuration dependence of the redshift space bispectrum for haloes in a LCDM cosmology. The configuration dependence is shown for the same triangle shapes and over the same scales as in Fig. 1. In all panels: solid (red) lines represent redshift space halo model predictions (HMs); dash (red) lines correspond to redshift space tree-level PT bispectra (PTs) [33]; and dotted (blue) lines correspond to real space tree-level PT predictions.

On intermediate scales $k_1 = 0.1\ h\,\mathrm{Mpc}^{-1}$, we see that both the PT and PTs predictions show an increased degree of configuration dependence, with the PT showing slightly more co-linear signal than the PTs. Again there is an amplitude off-set that should be understood as arising from Kaiser boosting. However, the HMs prediction now shows a strong departure from the PTs predictions, it having a much flatter configuration dependence. Recalling the same panel in Fig. 1, we see that this is due to the fact that the 3-Halo term is now competing with rising 2- and 1-Halo terms. Since the angular dependence of these terms appears to be relatively flat across the configuration, the result of adding them to the 3-Halo term is essentially to wash out the configuration dependence seen for the PT results. As noted in our analysis of Section IV C these terms act as effective shot-noise terms.

On smaller scales, $k_1 = 0.5\ h\,\mathrm{Mpc}^{-1}$, the trend noted previously for the PT and PTs predictions is continued. The HMs predictions are now very different than the PT ones and we see that there is a very strong configuration dependence emerging. The co-linear triangles show a significantly enhanced signal over the more equilateral like configurations, which have formed a broad plateau – this is the characteristic *U*-shape – which was first noted in the bispectrum by [33] and in the 3-point correlation function by [34]. Recalling Fig. 1 (bottom left panel), we see here that the prediction is completely dominated by the 1-Halo term, and so this *U*-shape feature is simply an imprint of the halo shape in redshift space – the FOG. On considering even more non-linear scales $k_1 = 1.0\ h\,\mathrm{Mpc}^{-1}$, we see, interestingly, that the result appears to be almost unchanged, except that the signal for co-linear configurations has slightly increased and also that the bottom of the *U* has become slightly broader. The amplitude at the base of the *U*, however, appears to be close to a constant value. However, from

our previous analysis of the small-scale limit in Section IV D, we see that a constant does not naturally emerge from the theory.

We note that since the scales over which we have investigated the configuration dependence are where current large scale structure surveys have most fidelity, models that do not include an accounting of the importance of the shot-noise terms or the virial motion induced FOG effect, must be treated with a degree of skepticism. The PTs theory is a clear example of this. Note that the FOG effects and effective 1- and 2-Halo shot-noise terms have an non-negligible impact on the bispectrum on scales that previously some would have considered accessible to by lowest-order perturbation theory.

On small scales, where our predictions are dominated by the 1-Halo term, the binning of the signal matters. Had we been careless, and averaged our results over relatively broad bins in θ_{12}, then we would have blurred out the imprint of the FOG distortions on the bispectrum. Our results show clearly this can not be the case – rather one expects the U-shape, at least for the dark matter in haloes in redshift space.

In this section we have shown from purely theoretical considerations that to use the galaxy bispectrum on large scales $k_1 < 0.1\,h\,\mathrm{Mpc}^{-1}$ as a precise tool for cosmology, one needs to understand exactly how to include the FOG effect and also how to correct for non-trivial discreteness effects. In the next section we confront our analytic model with numerical simulations.

VI. COMPARISON WITH NUMERICAL SIMULATIONS

A. Numerical simulations

In order to test our redshift space bispectrum we generated an ensemble of 8 LCDM simulations, these were identical in every way, except we drew different random realizations of the initial Fourier modes. The cosmological parameters for the ensemble were selected to be in broad agreement with the WMAP best fit model [5]: $\Omega_m = 0.27$, $\Omega_\Lambda = 0.73$, $\Omega_b = 0.046$, $h = 0.72$ and $\sigma_8(z=0) = 0.9$. We used the `cmbfast` [51] code to generate the linear theory transfer function, and we adopted the standard parameter choices, and took the transfer function output redshift to be at $z = 0$. The initial conditions for each simulation were then laid down at $z = 49$ using publicly available `2LPT` initial conditions generator [69, 70]. Subsequent gravitational evolution of the equations of motion was then performed using the publicly available `Gadget2` code [71]. Each simulation was run with $N = 400^3$ particles in a comoving volume of length $L = 512^3\mathrm{Mpc}h^{-1}$ and with a comoving force softening set to 70 kpc/h. The simulations were performed using a 4-way dual core Opteron processor system, and each ran to completion in roughly ∼1800 timesteps from redshift $z = 49$ to $z = 0$ and this translates to ∼2 days of wall clock time.

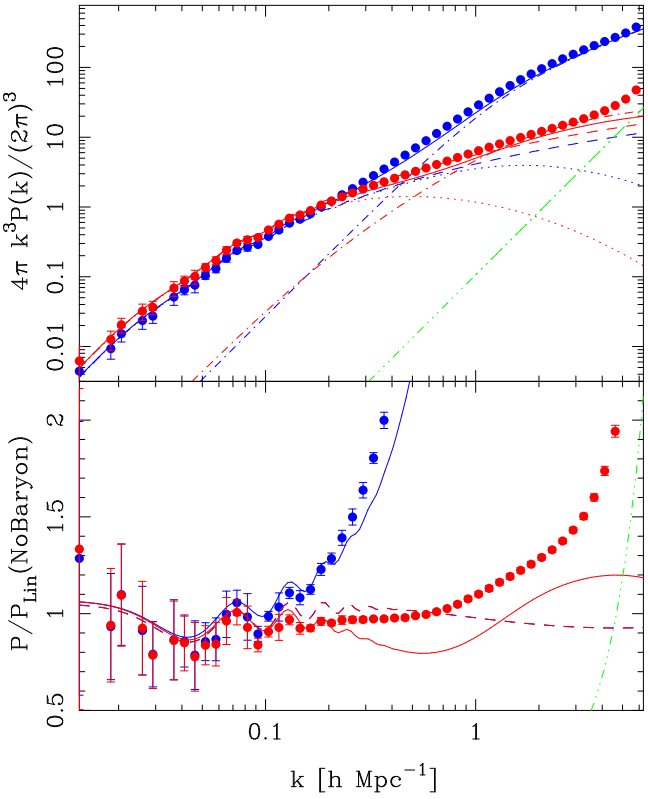

FIG. 3: Real and redshift space power spectrum of dark matter particles at $z = 0$ measured from the ensemble of LCDM simulations. Top panel: The power spectrum. Blue and red points show real and redshift space quantities, respectively. The solid, dot-dash and dotted lines show the total halo model, 1-Halo and 2-Halo terms. The triple dot-dash curve shows the predictions for the Poisson shot noise error. The dash line shows the linear theory. Bottom panel: The measured power spectra ratioed with a no-baryon linear theory power spectrum that has the same overall transfer function shape. Note that for the redshift space spectra, we have scaled out the Kaiser boost.

B. Estimating the power spectrum

To build up to our comparison of the analytic model with the numerical simulations we first compute the real and redshift space power spectra of the $z = 0$ outputs of the ensemble.

We estimate the density Fourier modes through the conventional Fast Fourier Transform (FFT) method: the dark matter particles were assigned to a regular cubical grid using the 'Cloud-In-Cell' (CIC) scheme [72]. The FFT of the gridded density field was then computed using the publicly available `FFTW` routines [73]. Each resulting Fourier mode was then corrected for the convolution with the mesh by dividing out the Fourier transform of the mass-assignment window function. For the CIC al-

gorithm this corresponds to the following operation:

$$\delta_{\rm d}(\mathbf{k}) = \delta_{\rm g}(\mathbf{k})/W_{\rm CIC}(\mathbf{k}) \ , \tag{55}$$

where

$$W_{\rm CIC}(\mathbf{k}) = \prod_{i=1,3} \left\{ \left[\frac{\sin\left[\pi k_i/2k_{\rm Ny}\right]}{\left[\pi k_i/2k_{\rm Ny}\right]} \right]^2 \right\} \tag{56}$$

where sub-script d and g denote discrete and grid quantities, and where $k_{\rm Ny} = \pi N_{\rm g}/L$ is the Nyquist frequency of the mesh and $N_{\rm g}$ is the number of grid cells.

The power spectra of the discrete particles on scale k_l are then estimated by performing the following sums,

$$\hat{P}_{\rm d}(k_l) = \frac{V_\mu}{M} \sum_{l=1}^{M} |\delta_{\rm d}(\mathbf{k}_l)|^2 \ , \tag{57}$$

where M is the number of Fourier modes in a spherical shell in k-space of thickness Δk. Note that the mode-by-mode correction differs from the analysis of [48, 74] where the correction for charge assignment was performed by computing the spherically averaged window and dividing it out. Mode-by-mode correction for the power spectrum was also performed in [36, 75, 76].

In Figure 3 we show the mean and 1-σ errors for the power spectrum of the dark matter particles in both real and redshift space, where the averages were taken over the 8 realizations. The spectra were computed using a 1024^3 FFT and we show all frequencies up to the Nyquist – the highest k-modes show signs of increased power from the Poison shot noise (triple dot-dash green line) and aliasing of power from smaller scales. We note that the large scale power shows a sequence of wiggles, these are the well known Baryonic Acoustic Oscillations (BAO) that have been discussed much in recent times [4, 36, 76, 77, 78, 79] – we shall not discuss these in this paper. The solid lines show the total halo model predictions for the real and redshift space. We see that whilst the real space model does reasonably well, with an accuracy of the order $< 10\%$, the redshift space predictions fare less well especially for scales $k > 0.2h{\rm Mpc}^{-1}$. Here the model systematically underpredicts the data by more than 20%.

These predictions are sensitive to the exact choice of how we model the FOG effects. Originally we used the relation between the velocity dispersion and mass given by Eq. (B12) with $\epsilon = 1$, however the predictions were particularly poor. We therefore investigated $M - \sigma_{\rm 1D}$ relation in the simulations. We found the haloes using a standard Friends-of-Friends (FoF) algorithm with link length $f = 0.2$. Fitting the velocity dispersions we found that $\epsilon = 1$ overpredicted the velocity dispersions by $> 20\%$. Fitting on ϵ we found that $\epsilon = 0.76$ provided a much better fit to this data (see Fig. 6). However, as Fig 3 shows, there must be other non-linear effects that are missing from the model. More precisely, the 2-Halo term in the redshift space power spectrum only includes linear halo motions – non-linear terms do contribute to this term (see [38, 79, 80]).

C. Estimating the bispectrum

Our estimator for the bin and spherical averaged bispectrum was developed following the work of [75], but with some changes. Our estimator can be written:

$$\begin{aligned} \hat{B}_{\rm d}(k_1, k_2, \theta_{12}) \ &= \ \frac{1}{V_1 V_2} \int_{V_1,\, V_2} \frac{d^3q_1}{(2\pi)^3} \frac{d^3q_2}{(2\pi)^3} \\ &\times \ B_{\rm d}(\mathbf{q}_1, \mathbf{q}_2, -\mathbf{q}_1 - \mathbf{q}_2) \ , \end{aligned} \tag{58}$$

where

$$V_i = \int_{k_i - \Delta k/2}^{k_i + \Delta k/2} \frac{d^3q}{(2\pi)^3} = \frac{4\pi k_i^2 \Delta k}{(2\pi)^3} \left[1 + \frac{(\Delta k)^2}{12 k_i^2} \right] \ . \tag{59}$$

A practical implementation of this estimator involves computing the following sum

$$\hat{B}_{\rm d} = \frac{V_\mu^2}{N_{\rm tri}} \sum_{\mathbf{n}_1, \mathbf{n}_2}^{N_{\rm tri}} \mathcal{R}e[\delta_{\rm d}(\mathbf{k}_{\mathbf{n}_1}) \delta_{\rm d}(\mathbf{k}_{\mathbf{n}_2}) \delta_{\rm d}(\mathbf{k}_{-\mathbf{n}_1 - \mathbf{n}_2})] \ , \tag{60}$$

where $\mathbf{n}_i$ is an integer vector from the k-space origin to a mesh point and so labels the modes, and where $N_{\rm tri}$ represents the number of independent momentum conserving k-vector triangles in the shells V_1 and V_2. In the above we take only the real part of the product of the three Fourier modes, owing to the reality of the bispectrum (see Eq. A21). Note that when computing the sum over k-space triangles, if the number of modes in a particular shell becomes larger than some threshold value, then we randomly sample from the set of triangles. Typically we limit the computations to 10000 modes per shell.

To accurately estimate Q we are also required to estimate the combination $Q_{\rm fac} \equiv P(k_1)P(k_2) + P(k_2)P(k_3) + P(k_3)P(k_1)$ for every k-space triangle that we use. There are two approaches to achieving this: we could simply estimate the power spectra in the k-space shells separately and form $Q_{\rm fac}$ after measuring B; or we can compute an estimate of $Q_{\rm fac}$ every time we estimate B, e.g. we accumulate

$$\begin{aligned} \hat{Q}_{\rm fac,\,d} \ &= \ \frac{V_\mu^2}{N_{\rm tri}} \sum_{\mathbf{n}_1, \mathbf{n}_2}^{N_{\rm tri}} \Big[|\delta_{\rm d}(\mathbf{k}_{\mathbf{n}_1})|^2 \, |\delta_{\rm d}(\mathbf{k}_{\mathbf{n}_2})|^2 \\ &+ |\delta_{\rm d}(\mathbf{k}_{\mathbf{n}_2})|^2 \, |\delta_{\rm d}(\mathbf{k}_{\mathbf{n}_3})|^2 + |\delta_{\rm d}(\mathbf{k}_{\mathbf{n}_3})|^2 \, |\delta_{\rm d}(\mathbf{k}_{\mathbf{n}_1})|^2 \Big] \ . \end{aligned} \tag{61}$$

We found that this latter technique was less noisy. This is due to the fact that only those modes that are used in estimating $\hat{B}_{\rm d}$, are used in estimating $\hat{Q}_{\rm fac,\,d}$, and this therefore reduces the sample variance.

In order to correct B and P for discreteness we also estimate the shot noise terms as [68]:

$$P_{\rm shot} \ \equiv \ \frac{V_\mu}{N} \ ; \tag{62}$$

$$B_{\rm shot} \ \equiv \ \frac{V_\mu}{N} \left[P_{\rm d}(k_1) + P_{\rm d}(k_2) + P_{\rm d}(k_3) \right] + \frac{V_\mu^2}{N^2} \ ; \tag{63}$$

$$Q_{\rm fac,\,shot} \ \equiv \ 2\frac{V_\mu}{N} \left[P_{\rm d}(k_1) + P_{\rm d}(k_2) + P_{\rm d}(k_3) \right] + 3\frac{V_\mu^2}{N^2} \ . \tag{64}$$

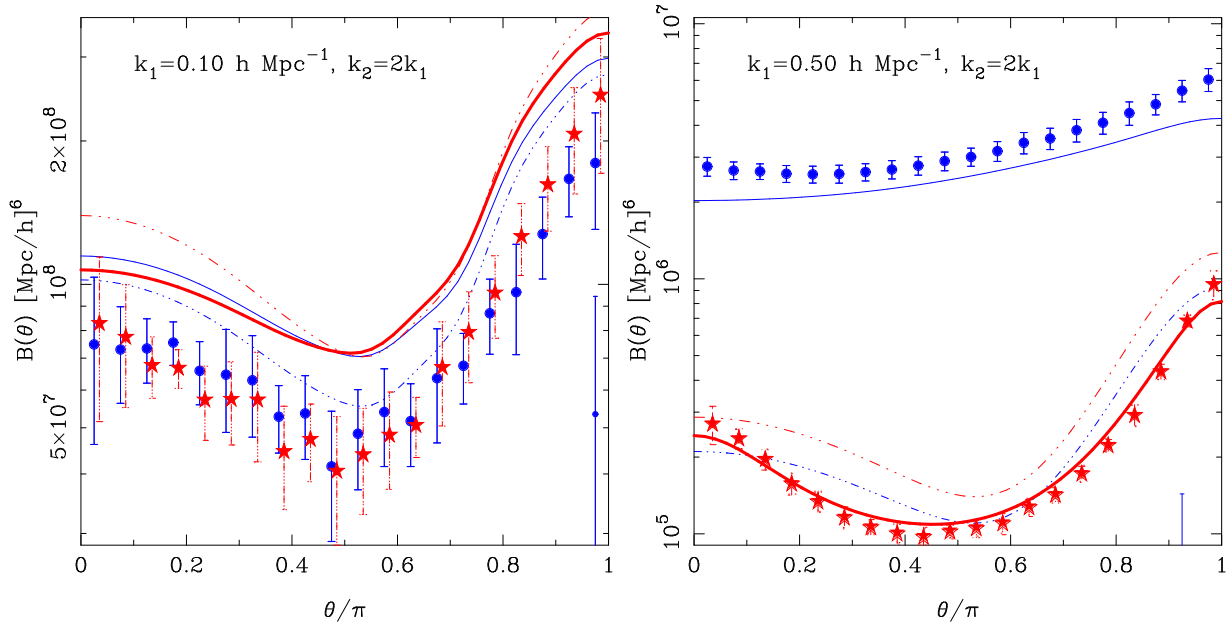

FIG. 4: Configuration dependence of the bispectrum in real and redshift space measured for the dark matter particles in the ensemble of LCDM simulations. Red and blue colors distinguish between real and redshift space quantities. The points with error bars show measurements: solid large points are for the real bispectrum; solid small points are for the imaginary bispectrum (which should be zero); open symbols are shot noise corrected estimates. The solid lines show the predictions from HM and HMs. The triple dot-dash lines show the predictions from PT and PTs. The two panels show the configuration dependence for k-space triangles with $k_2/k_1 = 2$ and for scales $k_1 = \{0.1, 0.5\}\, h\mathrm{Mpc}^{-1}$.

Estimates of the shot noise corrected continuous spectra are then arrived at through the following set of operations:

$$\hat{P} = \hat{P}_{\rm d} - P_{\rm shot} \ ; \quad (65)$$

$$\hat{B} = \hat{B}_{\rm d} - B_{\rm shot} \ ; \quad (66)$$

$$\hat{Q}_{\rm fac} = \hat{Q}_{\rm fac,\,d} - Q_{\rm fac,\,shot} \ ; \quad (67)$$

$$\hat{Q} = \hat{B}/\hat{Q}_{\rm fac} \ . \quad (68)$$

In our measurements we shall show both spectra with and without the shot noise corrections.

Lastly, as a consistency check for our estimates we also estimate the imaginary bispectrum, which is given by Eq. (60) only we take the imaginary piece of the product. Thus, if the estimate is correct, then this quantity should on average be zero. However, as the number of independent triangles becomes small the imaginary piece may become non-zero.

Figure 4 shows the mean and 1-σ errors for the configuration dependence of the bispectrum $B(k_1, k_2, \theta_{12})$ in both real and redshift space for the 8 LCDM simulations. The two panels show results for k-space triangles with $k_2/k_1 = 2$ and $k_1 = \{0.1, 0.5\} h\mathrm{Mpc}^{-1}$. Once again, blue and red colors distinguish between real and redshift space quantities.

Considering the largest scales first ($k = 0.1\, h\mathrm{Mpc}^{-1}$), we see that both the PT and PTs predictions overestimate the amplitude of the measured bispectra. The PT fares slightly better and the PTs slightly worse. However essentially all of the models get roughly the right configuration dependence which is encouraging. In the halo model the amplitude of this curve is also sensitive to the exact form chosen for the mass function and the concentration relation used for the density profiles.

On smaller scales ($k = 0.5\, h\mathrm{Mpc}^{-1}$), we see that both the HM and HMs models do significantly better than the PT and PTs models and well reproduce the configuration dependence, and in the case of the redshift space bispectrum also the amplitude. This very good agreement essentially means that our form for the 1-Halo term is correct and that the bispectrum on small scales is simply an imprint of the FOG distortions.

Figure 5 shows results for the configuration dependence of the reduced bispectrum, $Q(k_1, k_2, \theta_{12})$ with (large open symbols) and without (large solid symbols) shot noise correction. The small symbols show the imaginary bispectrum. Considering again the largest scales ($k = 0.1\, h\mathrm{Mpc}^{-1}$), we see that neither the HM nor the PT predictions give the same amplitude as the estimates from simulations. In both models the discrepancy owes to the amplitude off-set from the bispectrum as discussed above, since the power spectra on these scales are reasonably well modeled. However, all the predictions describe the shape of the configuration dependence reasonably well, which shows an excess of signal for co-linear triangles. This means that the FOG are playing relatively little role on these scales and we are essentially probing the large scale filamentary structures in both real and

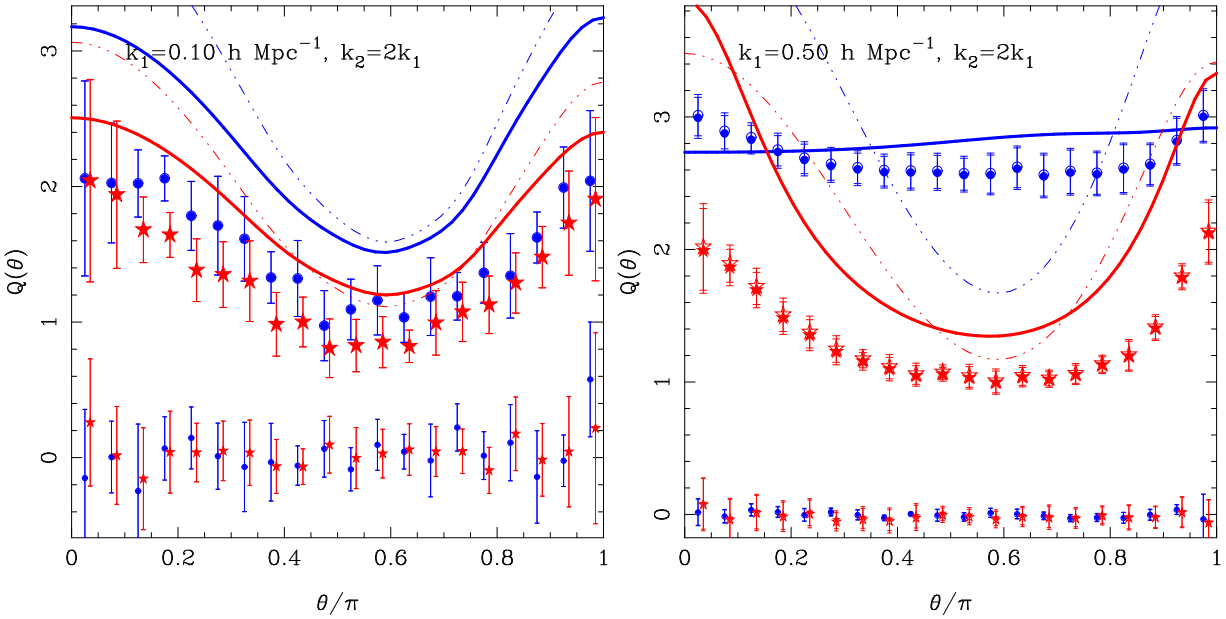

FIG. 5: Same as Fig. 4 only this time for the reduced bispectrum.

redshift space [33, 75]. The HM does have less configuration dependence owing to the enhanced shot-noise, which is flat across the configuration.

Considering smaller scales ($k = 0.5\,h\mathrm{Mpc}^{-1}$) we see that the real space measurements have increased in amplitude and become flat across the configuration – this agrees rather well with the HM predictions, and implies that the statistic is already in the fully non-linear regime. We therefore should think that the redshift space bispectrum must also be fully non-linear. However, the configuration dependence has not changed much. Here the failure of the HMs to predict the correct amplitude appears to be due to the fact that the prediction for the power spectrum is $\sim 20\%$ too low (hence making the prediction for $Q_{\rm fac}$ too small). Achieving better agreement in the power should mitigate this discrepancy.

Lastly, the small discrepancies between the real space HM predictions and the simulations, are entirely consistent with the work of [19] – in real space haloes are triaxial and not spherical and this shows up as a characteristic mark in the configuration dependence.

VII. TOWARDS THE REDSHIFT SPACE 3-POINT CORRELATION FUNCTION

In this section we discuss how our model for the bispectrum can be used to generate predictions for the redshift space 3-point correlation function.

A. Spherical Harmonic representation

In principle, the 3-point correlation function is related to the bispectrum by two 3-D Fourier transforms. Since B^s requires four integrals, it would appear that ξ^s_3 requires the evaluation of 10-D integrals—this is currently prohibitively expensive. Fortunately, as was first pointed out by [81, 82, 83], significant simplifications can be made if B^s satisfies certain symmetry conditions .

Consider the isotropized bispectrum, which is completely specified by the lengths of two sides of a triangle (k_1, k_2) and the angle between those lengths μ_{12}. Therefore, we may write it as a sum over Legendre polynomials:

$$\hat{B}^s(k_1,k_2,\mu_{12}) = \sum_{l=0}^{\infty} \mathcal{P}_l(\mu_{12})\, B^s_l(k_1,k_2)\ ;$$
$$B^s_l(k_1,k_2) = \frac{2l+1}{2}\int_{-1}^{1} d\mu_{12}\, \mathcal{P}_l(\mu_{12}) \hat{B}^s(k_1,k_2,\mu_{12})\ , \tag{69}$$

where the multipole coefficients, $B^s_l(k_1,k_2)$, are obtained from the orthogonality of the Legendre polynomials. Since the isotropic bispectrum is rotationally invariant, so is the 3-point correlation function (See Appendix A). It therefore also has a multipole expansion:

$$\hat{\zeta}^s(r_{13},r_{23},\mu_\alpha) = \sum_{l=0}^{\infty} \mathcal{P}_l(\mu_\alpha)\, \zeta^s_l(r_{13},r_{23})_l\ ;$$
$$\zeta^s_l(r_{13},r_{23}) = \frac{2l+1}{2}\int_{-1}^{1} d\mu_\alpha\, \mathcal{P}_l(\mu_\alpha)\, \hat{\zeta}^s(r_{13},r_{23},\mu_\alpha)\ . \tag{70}$$

The next step is to relate the multipole coefficients of the 3-point function to those of the bispectrum.

Following [81, 82, 83], we firstly insert our multipole representation for the bispectrum into Eq. (A14), which is the formal relation between the 3-point function and the bispectrum. Next, we take advantage of the spherical harmonic representation for the plane wave and substitute this into our expressions. We may also make use of the addition theorem for spherical harmonics to re-write the Legendre polynomial in θ_{12} as a sum over products of spherical harmonics with the dependence on (θ_1, ϕ_1) and (θ_2, ϕ_2). The orthogonality of the spherical harmonics allows us to perform the surface integrals over the unit vectors of $\mathbf{k}_1$ and $\mathbf{k}_2$ directly. On completing these operations we arrive at the exact expression,

$$\zeta^s_l(r_{13}, r_{23}) \;=\; (-1)^l \int \frac{dk_1}{2\pi^2}\,\frac{dk_2}{2\pi^2}\,k_1^2\,k_2^2 \times B^s_l(k_1,k_2)\,j_l(k_1 r_{13})\,j_l(k_2 r_{23})\;. \quad (71)$$

Hence, given the isotropic bispectrum, the 3-point correlation function is simply a series sum of 2-D integrals of the bispectrum multipoles. Thus to compute the redshift space 3-point correlation function we are required to perform: a 4-D integral to obtain the bispectrum, followed by a set of 1-D integrals to obtain the multipoles, and finally a set of 2-D integrals to obtain the correlation function multipoles. If the angular dependence of the bispectrum is closely approximated by a polynomial of order l', then all $l > l'$ multipoles will be vanishingly small. In practice this may be achieved by requiring

$$\frac{[\zeta^s(r_{13}, r_{23}]_{l'+1}}{[\zeta^s(r_{13}, r_{23}]_0} < \epsilon\;, \quad (72)$$

where ϵ is smaller than the measurement errors.

In principle, the number of terms in the multipole series may be very large, however we note that, at least in real space, this approach has been successfully performed [83], and the configuration dependence was captured after a relatively small number of multipoles and this obviates the need for approximate forms for the real space correlation function [53]. However, we know of no attempt to perform this procedure in the redshift space. That this approach can be practically implemented, shall be left as a task for future research.

VIII. CONCLUSIONS

In this paper, we have provided a new analytic model for the redshift space bispectrum of dark matter, haloes and galaxies in the plane parallel approximation for the redshift space distortion. On large scales, the model predictions have a direct correspondence to the non-linear perturbation theory and on small scales, the predictions are entirely governed by the phase space density of galaxies/dark matter internal to the haloes. This is the first time that the information from bulk flows and virial motions have been naturally incorporated into an analytic model for the higher-order clustering statistics in redshift space.

In our analytic model the bispectrum is represented as a sum over three distinct terms; these correspond to all of the possible distinct arrangements of three points in three haloes, and we referred to these as the 1-, 2- and 3-Halo terms. A practical evaluation of the isotropic bispectrum (the direct observable), with realistic models for halo profiles, abundance and clustering, required the execution of a set of 4-D numerical integrals. For the terms that involved large-scale correlations (2- and 3-Halo terms) it was shown that these expressions could be easily modularized, and so are best computed in parallel. The 1-Halo term must be integrated with an efficient higher-dimensional integrator.

It was further shown that the large-scale predictions in the model, which are governed by the 2- and 3-Halo terms, can be simplified greatly under the approximation that the angle average of the product of anisotropic density profiles and large scale clustering of halo centers can be performed separately. Results for the numerical integration of the exact and approximate expressions were computed. These showed that the approximation worked extremely well on large and small scales; on intermediate scales it is within 7% of the exact Halo Model answer.

The predictions of our isotropic bispectrum calculation were then compared with the analytic PT in real and redshift space. On very large scales $k = 0.01h\mathrm{Mpc}^{-1}$ our model closely agrees with the redshift space PT predictions, but there are some small deviations in the configuration dependence. These were attributed to the 'effective' shot-noise terms that arise from the discreteness of the halo field, although we caution that the low-k limit of the 1- and 2-Halo terms may not be reliable enough [49] to take this at face value.

On smaller, but still large scales $k = 0.1h\mathrm{Mpc}^{-1}$ we showed that our analytic model showed a dramatic departure from the PT predictions – it shows a flatter configuration dependence. Again this was attributed to the effective shot-noise terms in our model. On mildly non-linear to fully non-linear scales we demonstrated that the configuration dependence of the bispectrum took on the characteristic *U*-shape anisotropy previously noted in the bispectrum by [33] and then later in 3-point correlation function measurements by [27, 34]. This was the imprint in the configuration dependence of the FOG distortions from non-linear virial motions – and by $k = 0.5h\mathrm{Mpc}^{-1}$ no imprint of the PT remained in our Halo Model predictions.

Our model predictions also allowed us to note that: there was no apparent scale where a hierarchical model provided a good description of the configuration dependence of the bispectrum. Thus, if our model predictions are correct, then such scalings are strongly disfavored in the halo model framework. However, in the non-linear regime, the *U*-shape appears as a generic pre-

diction. However, how sensitive its shape is to cosmology and the velocity distribution, still remains to be determined.

We then confronted our predictions with measurements from numerical simulations. We found that on large scales, $k = 0.1\,h\mathrm{Mpc}^{-1}$, the PT and halo model predicted the correct configuration dependence, however had amplitudes that were roughly $\sim 20\%$ too high. If correct, this leads us to conclude that studies which use the lowest order PT to extract galaxy bias are unlikely to be robust on these scales – higher order terms will be necessary for good agreement. This agrees with the findings of [33, 75]. On smaller scales, $k = 0.5\,h\mathrm{Mpc}^{-1}$, our analytic model matched well the measurements, significantly improving on the PT model.

We then showed how one may use our analytic model to generate predictions for the redshift space 3-point correlation function. The method was built on the idea that one may apply the spherical harmonic decomposition of 3-point functions, just as for real space statistics [81, 82, 83], to the isotropic bispectrum. This emphasized why obtaining analytic forms for the isotropic bispectrum is important. However it remains to be seen whether or not this method can be turned into a practical procedure for computing the 3-point function multipoles.

In future work, we shall extend our analysis to examine the halo and galaxy clustering as a function of mass and type. It will be also important to resolve whether or not the Halo Model's effective shot-noise terms are important for modeling real survey data. Owing to the fact that different galaxy populations are easily and naturally included into our description, it is hoped that this approach will help to facilitate extraction of information from current and future hi-fidelity large scale structure surveys of the Universe.

Acknowledgments

The authors thank Uros Seljak, Bhuvnesh Jain, Laura Marian, Cameron McBride and Bob Nichol for useful discussions. RES and RKS acknowledge support from the National Science Foundation under Grant No. 0520647. RS is partially supported by NSF AST-0607747 and NASA NNG06GH21G.

APPENDIX A: DUALITY OF CLUSTERING STATISTICS

This section defines the configuration and Fourier space clustering statistics and their dual relationship with one another. It also shows how the cosmological assumptions impose certain important conditions upon these statistics.

We shall assume that ensemble averages are taken over a volume, V_μ, of the Universe sufficiently large for the fundamental k-space cell volume to be considered infinitesimally small; outside of this large volume our stochastic fields are exactly zero. This allows us to define Fourier transforms in the volume. We shall also let these fields be Ergodic, whence ensemble averages are equivalent to averages over volume.

1. Real space representation: correlation functions

The fractional density field of matter is defined:

$$\delta(\mathbf{x},t) \equiv [\rho(\mathbf{x},t) - \bar{\rho}(t)]/\bar{\rho}(t)\ , \tag{A1}$$

where $\rho(\mathbf{x},t)$ is the local density at coordinates $(\mathbf{x},t)$ and $\bar{\rho}(t)$ is the density of the homogeneous background at time t. The n-point connected auto-correlation functions of δ, represent the excess probability from the product of the individual independent 1-point distributions of obtaining a particular set of values at all points, e.g. the probability of obtaining fluctuations at three points (a,b,c) can be written:

$$P(a,b,c) \equiv P(a)P(b)P(c)\left[1 + C_2(a,b) + C_2(b,c) + C_2(c,a) + C_3(a,b,c)\right]\ . \tag{A2}$$

where C_2 and C_3 are the connected 2– and 3–point correlation functions. We may now be clear about what we mean by connected correlation function: the connected correlator may not be reduced to sums over products of lower order connected correlators. In cosmology these are more commonly written:

$$\xi_2(\mathbf{x}_1,\mathbf{x}_2|t) \equiv \langle\delta(\mathbf{x}_1,t)\,\delta(\mathbf{x}_2,t)\rangle_c\ ; \tag{A3}$$

$$\xi_3(\mathbf{x}_1,\mathbf{x}_2,\mathbf{x}_3|t) \equiv \langle\delta(\mathbf{x}_1,t)\,\ldots\,\delta(\mathbf{x}_3,t)\rangle_c\ ; \tag{A4}$$

$$\xi_n(\mathbf{x}_1,\ldots,\mathbf{x}_n|t) \equiv \langle\delta(\mathbf{x}_1,t)\,\ldots\,\delta(\mathbf{x}_n,t)\rangle_c\ . \tag{A5}$$

These functions obey an integral constraint

$$\frac{1}{V_\mu}\int d^3x_n \xi_n(\mathbf{x}_1,\ldots,\mathbf{x}_n) \to 0 \ ; \ n>1 \ . \tag{A6}$$

This follows from noting that on marginalizing the probability functions over one variable, say the Nth variable, one finds that the resulting distribution depends on $n-1$-points, and therefore from Eq. (A2) must not depend on the n-point connected correlation function.

If the density field obeys the cosmological principle, that is statistical homogeneity and isotropy on scales greater than the coherence scale of our fields, then the correlation functions are invariant under translation and rotation of the coordinate system. They are also parity invariant real functions and are invariant to exchange of vector arguments. Thus:

$$\begin{aligned}
\xi_n(\mathbf{x}_1,\ldots,\mathbf{x}_n) &= \xi_n(\mathbf{x}_1+\mathbf{x}_0,\ldots,\mathbf{x}_n+\mathbf{x}_0) \quad \text{(Translation)} \ ; & \text{(A7)}\\
&= \xi_n(\mathcal{R}\mathbf{x}_1,\ldots,\mathcal{R}\mathbf{x}_n) \quad \text{(Rotation)} \ ; & \text{(A8)}\\
&= \xi_n(-\mathbf{x}_1,\ldots,-\mathbf{x}_n) \quad \text{(Parity)} \ ; & \text{(A9)}\\
&= \xi_n(\mathbf{x}_2,\mathbf{x}_1,\ldots,\mathbf{x}_n) \quad \text{(Exchange)} \ ; & \\
&= \xi_n(\mathbf{x}_i,\mathbf{x}_2,\ldots\mathbf{x}_1,\ldots,\mathbf{x}_n) & \text{(A10)}
\end{aligned}$$

For anisotropic fields rotation invariance is broken and for inhomogeneous fields translation symmetry is broken. For homogeneous fields we may immediately apply the translational invariance and drop one of the vector arguments in our function. Setting $\mathbf{x}_0=-\mathbf{x}_n$ in Eq. (A7) gives,

$$\xi_n(\mathbf{x}_1,\ldots,\mathbf{x}_n)=\xi_n(\mathbf{x}_{1n},\ldots,\mathbf{x}_{(n-1)n}) \ , \tag{A11}$$

where $\mathbf{x}_{ij}\equiv\mathbf{x}_i-\mathbf{x}_j$ and we shall not write the zero argument in the nth space. In this paper we will mainly be concerned with clustering statistics that obey homogeneity, but are anisotropic, as this is exactly the case for the redshift space distortion in the plane parallel approximation. Lastly, we have the closure relation: $\mathbf{x}_{21}+\mathbf{x}_{32}+\cdots+\mathbf{x}_{1n}=\mathbf{0}$.

2. Fourier space representation: poly-spectra

Under the conditions stated earlier, the density field $\delta(\mathbf{x},t)$ may be equivalently written as an infinite sum over plane waves through the Fourier transform, where our Fourier convention is

$$\delta(\mathbf{x})=\frac{V_\mu}{(2\pi)^3}\int d^3k\delta(\mathbf{k})e^{-i\mathbf{k}\cdot\mathbf{x}} \ \Leftrightarrow \ \delta(\mathbf{k})=\frac{1}{V_\mu}\int d^3x\,\delta(\mathbf{x})e^{i\mathbf{k}\cdot\mathbf{x}} \ . \tag{A12}$$

Transforming the density terms in Eqs (A3–A5), leads to

$$\xi_2(\mathbf{r}_{12}) = \int\prod_{i=1}^{1}\left\{\frac{d^3k_i}{(2\pi)^3}\right\}P_2(\mathbf{k}_1,\mathbf{k}_2)e^{-i\mathbf{k}_1\cdot\mathbf{r}_{12}} \ ; \quad [\mathbf{k}_1+\mathbf{k}_2=\mathbf{0}] \tag{A13}$$

$$\xi_3(\mathbf{r}_{13},\mathbf{r}_{23}) = \int\prod_{i=1}^{2}\left\{\frac{d^3k_i}{(2\pi)^3}\right\}P_3(\mathbf{k}_1,\mathbf{k}_2,\mathbf{k}_3)e^{-i\mathbf{k}_1\cdot\mathbf{r}_{13}-i\mathbf{k}_2\cdot\mathbf{r}_{23}} \ ; \quad [\mathbf{k}_1+\mathbf{k}_2+\mathbf{k}_3=\mathbf{0}] \tag{A14}$$

$$\xi_n(\mathbf{r}_{1n},\ldots,\mathbf{r}_{(n-1)n}) = \int\prod_{i=1}^{n-1}\left\{\frac{d^3k_i}{(2\pi)^3}\right\}P_n(\mathbf{k}_1,\ldots,\mathbf{k}_n)e^{-i\mathbf{k}_1\cdot\mathbf{r}_{1n}-\cdots-i\mathbf{k}_{(n-1)}\cdot\mathbf{r}_{(n-1)n}} \ ; \quad \left[\sum_{i=1}^{n}\mathbf{k}_i=\mathbf{0}\right] \tag{A15}$$

where we have very generally defined the n-point spectrum as:

$$V_\mu^{n-1}\left\langle\delta^s(\mathbf{k}_1)\ldots\delta^s(\mathbf{k}_n)\right\rangle=P_n^s(\mathbf{k}_1,\ldots,\mathbf{k}_n)\left[\delta^D_{1\ldots n}\right](2\pi)^3/V_\mu \ , \tag{A16}$$

this condition simply arises from the imposed harmonic boundary conditions within our volume: only overlapping waves are constructive. The short hand notation $\left[\delta^D_{12\ldots}\right]\equiv\delta^D(\mathbf{k}_1+\mathbf{k}_2+\ldots)$ has been adopted for the argument of the Dirac delta function. The presence of this term ensures that the sum of k-vectors forms a null vector, $\mathbf{k}_1+\cdots+\mathbf{k}_n=\mathbf{0}$ and we shall refer to this as the closure condition. For the case of $(n=2)$, we have the power spectrum $P_2(\mathbf{k}_1,\mathbf{k}_2)\equiv P(\mathbf{k}_1)$ and for $(n=3)$ we have the bispectrum $P_3(\mathbf{k}_1,\mathbf{k}_2,\mathbf{k}_3)\equiv B(\mathbf{k}_1,\mathbf{k}_2,\mathbf{k}_3)$.

Conversely, the power spectra may also be written as inverse Fourier transforms of the correlation functions:

$$P(\mathbf{k}_1) = \int d^3\mathbf{r}_{12}\, \xi(\mathbf{r}_{12}) e^{i\mathbf{k}_1\cdot\mathbf{r}_{12}} \; ; \tag{A17}$$

$$B(\mathbf{k}_1,\mathbf{k}_2,\mathbf{k}_3) = \int d^3\mathbf{r}_{13}\, d^3\mathbf{r}_{23}\, \zeta(\mathbf{r}_{13},\mathbf{r}_{23})\, e^{i[\mathbf{k}_1\cdot\mathbf{r}_{13}+\mathbf{k}_2\cdot\mathbf{r}_{23}]}, \tag{A18}$$

$$P_n(\mathbf{k}_1,\ldots,\mathbf{k}_n) = \int d^3\mathbf{r}_{1n}\, \ldots d^3\mathbf{r}_{(n-1)n}\, \xi_n(\mathbf{r}_{1n},\ldots,\mathbf{r}_{(n-1)n})\, e^{i\left[\mathbf{k}_1\cdot\mathbf{r}_{1n}+\cdots+\mathbf{k}_{(n-1)}\cdot\mathbf{r}_{(n-1)n}\right]} \; . \tag{A19}$$

From these relations and the properties of the correlation functions, Eqs (A7–A10), we may now infer the corresponding properties for the poly-spectra. Translational invariance in configuration space means that the poly-spectra are invariant under a phase shift to the Fourier density fields. Invariance to rotation of the coordinate frame leads to rotation invariance of the polyspectra:

$$\begin{aligned} P_n(\mathbf{k}_1,\ldots,\mathbf{k}_n) &= \int d^3[\mathcal{R}\mathbf{r}_{1n}]\, \ldots d^3[\mathcal{R}\mathbf{r}_{(n-1)n}]\, \xi_n(\mathcal{R}\mathbf{r}_{1n},\ldots,\mathcal{R}\mathbf{r}_{(n-1)n})\, e^{i\left[\mathbf{k}_1^T\mathcal{R}\mathbf{r}_{1n}+\cdots+\mathbf{k}_{(n-1)}^T\mathcal{R}\mathbf{r}_{(n-1)n}\right]} \; , \\ &= \int d^3\mathbf{r}_{1n}\, \ldots d^3\mathbf{r}_{(n-1)n}\, \xi_n(\mathbf{r}_{1n},\ldots,\mathbf{r}_{(n-1)n})\, e^{i\left[\mathbf{r}_{1n}^{\mathrm{T}}\mathcal{R}^{\mathrm{T}}\mathbf{k}_1+\cdots+\mathbf{r}_{(n-1)n}^{\mathrm{T}}\mathcal{R}^{\mathrm{T}}\mathbf{k}_{(n-1)}\right]} \\ &= P_n(\mathcal{R}^{\mathrm{T}}\mathbf{k}_1,\ldots,\mathcal{R}^{\mathrm{T}}\mathbf{k}_n) \end{aligned} \tag{A20}$$

Parity invariance and the reality of the configuration space functions leads to the reality of the poly-spectra:

$$P_n(\mathbf{k}_1,\ldots,\mathbf{k}_n) = P_n(-\mathbf{k}_1,\ldots,-\mathbf{k}_n) = \overline{P}_n(\mathbf{k}_1,\ldots,\mathbf{k}_n) \; , \tag{A21}$$

where the over-line corresponds to complex conjugation. Many of these properties simplify the analysis in the main text.

APPENDIX B: CALCULATIONAL DETAILS

1. The NFW density profile with the Bullock et al. normalization

As described in Section III B to compute the redshift space density profile we require a model for the real space density profile $\rho(r)$ and a model for the 1-point velocity distribution function of particles in a halo. For the density profile we adopt the 'NFW' model [84]:

$$\rho(r) = \rho_c \left[y(1+y)^2\right]^{-1} \; ; \quad y \equiv r/r_c \; . \tag{B1}$$

This model is fully determined by two parameters, ρ_c and r_c, a characteristic density and radius. These two parameters are not independent, but are related by the mass enclosed:

$$\rho_c = \frac{\bar{\rho}\Delta_{\rm vir}c^3/3}{\log(1+c)-c/(1+c)} \; ; \quad c \equiv \frac{r_{\rm vir}}{r_c} \; , \tag{B2}$$

where c is the concentration parameter and is the ratio of the virial radius to the characteristic radius. The virial radius is the boundary layer within which all particles have undergone violent non-linear relaxation. It is taken to be specified through

$$M_{\rm vir} = \frac{4}{3}\pi r_{\rm vir}^3 \Delta_{\rm vir}\bar{\rho} \; , \; . \tag{B3}$$

$\Delta_{\rm vir}$ is the density contrast for virialization, which may be estimated from the spherical collapse model. For flat universes with a cosmological constant a good fit to the functional form is provided by [85]

$$\Delta_{\rm vir} = \left[(18\pi^2 + 82x - 39x^2\right]/\Omega(a) \; ; \quad x \equiv [\Omega(a)-1] \; . \tag{B4}$$

To obtain the concentration parameter as a function of mass we follow the model of Bullock et al. [86]. For this we have

$$c = K\frac{a}{a_c(M_{\rm vir})} \tag{B5}$$

where we take $K = 3.0$ and where $a_c(M_{\rm vir})$ is the collapse expansion factor for a halo of mass $M_{\rm vir}$. The collapse expansion factor for a halo of mass M may be determined through solving the relation

$$\frac{D_1(a_c)}{D_1(a_0)}\sigma(FM_{\rm vir}, a_0) = \delta_c \ , \tag{B6}$$

where $F = 0.001$ is taken as a fixed fraction of the initial mass, $D(a)$ is the linear theory growth factor at epoch a. The parameter $\delta_c = 1.686$ is the linearly extrapolated density threshold for collapse from the spherical collapse model, where we ignore the slight dependence on cosmology [87]. As was shown by [86] this model provides a very good description of the ensemble average properties of dark matter haloes. More sophisticated models may be constructed that take into account that haloes are more complicated, e.g. a halo of mass M drawn at random from the ensemble will have a concentration parameter that is drawn from a probability distribution of possible concentrations. In addition one may include sub-structure [88] or halo triaxiality [19, 65]. However, we shall leave these additional embellishments for future study.

2. Conversion between Sheth & Tormen and Bullock et al mass defintions

The definitions of halo mass that are used in the Sheth & Tormen mass function and the Bullock et al. model for the density profile are inconsistent. We recall that the Sheth & Tormen halo mass is defined:

$$M_{\rm ST} = \frac{4}{3}\pi r_{\rm ST}^3 200\bar{\rho} \ . \tag{B7}$$

We resolve this inconsistency using the methodology of [65], which briefly is as follows: For a given halo of the NFW type, the physical values of the characteristic density and radius are independent of our specific choice of halo mass. Using the relation for the physical density as a constant we arrive at the mapping

$$\left(\frac{c_{\rm vir}}{c_{\rm ST}}\right)^3 = \frac{200}{\Delta_{\rm vir}}\left[\frac{\log(1+c_{\rm vir}) - c_{\rm vir}/(1+c_{\rm vir})}{\log(1+c_{\rm ST}) - c_{\rm ST}/(1+c_{\rm ST})}\right] \ . \tag{B8}$$

Thus if we take a Bullock et al. mass and derive the appropriate $c_{\rm vir}$ we may then solve the above expression to find $c_{\rm ST}$. Following this we may then obtain the corresponding Sheth & Tormen mass through application of the relation,

$$M_{\rm ST} = \frac{200}{\Delta_{\rm vir}}\left(\frac{c_{\rm ST}}{c_{\rm vir}}\right)^3 M_{\rm vir} \ . \tag{B9}$$

3. 1-Point velocity distribution profile

For the 1D velocity distribution function we adopt the standard Maxwellian distribution [39, 40, 41, 89]:

$$\mathcal{V}[u_z|\sigma_{\rm 1D}(M_{\rm vir})]du_z = \frac{1}{\sqrt{2\pi}\sigma_{\rm 1D}}\exp\left[-\frac{u_z^2}{2\sigma_{\rm 1D}^2}\right]du_z \ , \tag{B10}$$

where $\sigma_{\rm 1D}$ is the 1D velocity dispersion. For haloes that possess an isothermal density distribution, this quantity is related to the halo circular velocity (V_c) through the following relation [90]

$$\sigma_{\rm 1D}^2(M_{\rm vir}) = \epsilon V_c^2/2 \ ; \qquad V_c^2 = \frac{GM_{\rm vir}}{r_{\rm vir}} \tag{B11}$$

Note that we have included a parameter ϵ into Eq. (B11), this may be used to account for the fact that the relation is only approximately true for the NFW density profile model. It also serves the further purpose of allowing us to turn off the fingers-of-god through setting $\epsilon \to \eta \ll 1$. As discussed in Section VI B and shown in Fig 6 $\epsilon = 0.76$ provides a reasonable fit to the velocity dispersion mass relation from simulations. On combining the above relations we have

$$\sigma_{\rm 1D}^2(M_{\rm vir}) = \frac{100\,\epsilon}{2}\,\Omega_m(a)\left[H(a)\,r_{\rm vir}\right]^2 \ , \tag{B12}$$

Notice that the ratio $\sigma_{\rm 1D}(M_{\rm vir})/r_{\rm vir}$ is independent of halo mass. One immediate consequence of this is that in redshift space the ratio of the line-of-sight projection of particles in a halo compared to the transverse length will be

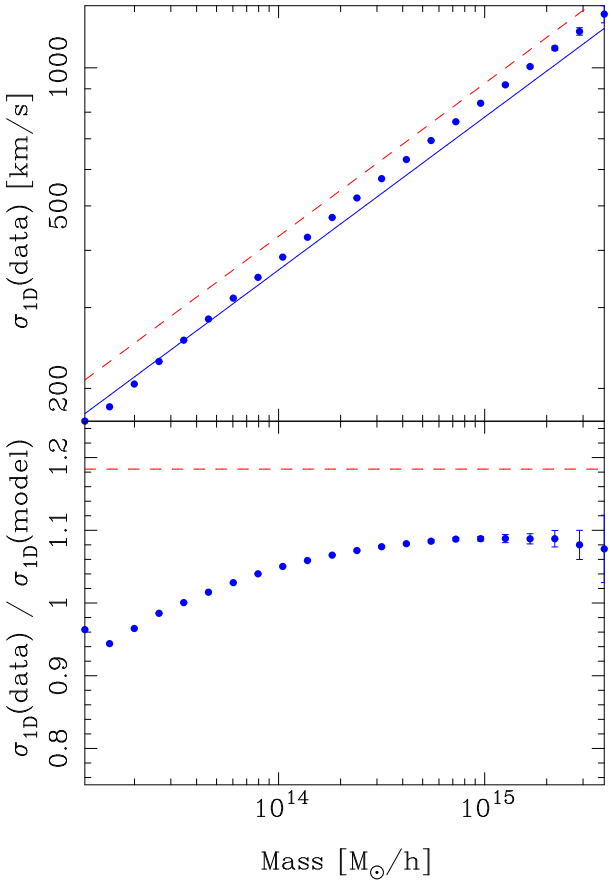

FIG. 6: Mass verses 1D velocity dispersion measured for FoF haloes in simulations. Points show mean and 1-sigma errors for measurements from the numerical simulations. The solid and dash line shows the predictions from Eq. B12 with $\epsilon = \{0.76, 1.0\}$. The bottom panel shows the ratio of the data with respect to the $\epsilon = 0.76$ model.

a constant, $\sigma_{\rm 1D}/(Hr_{\rm vir}) \sim 3$, regardless of mass. In other words, FOGs lead to density profiles which are self-similar. In our analysis we take $\epsilon = 0.76$ (See Fig. 6). Finally, the Fourier transform of the velocity distribution is

$$\mathcal{V}(\mu_1 k_1) = \exp\left\{-\frac{1}{2}[k_1\mu_1\sigma_{\rm 1D}(M_{\rm vir})]^2\right\} \ . \tag{B13}$$

APPENDIX C: EULERIAN PT AND HALO-PT KERNELS

The first two symmetrized Eulerian PT kernels for the density and divergence of the velocity field are [6]:

$$F_{1,2} = \frac{5}{7} + \frac{\mu_{12}}{2}\left[\frac{q_1}{q_2} + \frac{q_2}{q_1}\right] + \frac{2(\mu_{12})^2}{7} \ ; \tag{C1}$$

$$G_{1,2} = \frac{3}{7} + \frac{\mu_{12}}{2}\left[\frac{q_1}{q_2} + \frac{q_2}{q_1}\right] + \frac{4(\mu_{12})^2}{7} \ , \tag{C2}$$

where $F_{1,\ldots,j} \equiv F_j(\mathbf{q}_1, \ldots, \mathbf{q}_j)$ and where $\mu_{12} \equiv \mathbf{q}_1 \cdot \mathbf{q}_2/q_1q_2$.

The Halo-PT kernels, symmetrized in all of their arguments, may be written in terms of the Eulerian PT kernels up to 2nd order as [36]:

$$F_0^{\rm hc} = b_0(M) \ ; \tag{C3}$$

$$F_1^{\rm hc} = b_1(M)W(|\mathbf{k}|R)F_1 \ ; \tag{C4}$$

$$F_{1,2}^{\rm hc} = b_1(M)W(|\mathbf{k}|R)F_{1,2} + \frac{b_2(M)}{2}W(|\mathbf{q}_1|R)W(|\mathbf{q}_2|R)F_1F_2 \tag{C5}$$

where $F^{\rm hc}_{1,..,j} \equiv F^{\rm hc}_j(\mathbf{q}_1,\ldots,\mathbf{q}_j|M,R)$ and where $\mathbf{k}=\mathbf{q}_1+\cdots+\mathbf{q}_j$.

APPENDIX D: ROTATION MATRIX

Owing to there being several equivalent ways to define the Euler angles and hence the rotation matrix $\mathcal{R}(\gamma_1,\gamma_2,\gamma_3)$, we make explicit our adopted choice. The angles are defined as follows: γ_1 describes a rotation of the coordinate system around the z-axis; γ_2 a rotation around the new y'-axis; and γ_3 a rotation around the new z''-axis ([91]). Thus, the components of any vector $\mathbf{k}$ specified in some initial Cartesian system can be transformed into the scalar components of the new rotated basis vectors through $\mathbf{k}'=\mathcal{R}(\gamma_1,\gamma_2,\gamma_3)\mathbf{k}$. The $z-y'-z''$ rotation matrix is [91]:

$$\mathcal{R}(\gamma_1,\gamma_2,\gamma_3) \equiv \begin{pmatrix} [C\gamma_2\, C\gamma_1 C\gamma_3 - S\gamma_1\, S\gamma_3] & [C\gamma_2\, S\gamma_1\, C\gamma_3 + C\gamma_1\, S\gamma_3] & -S\gamma_2\, C\gamma_3 \\ [-C\gamma_2\, C\gamma_1\, S\gamma_3 - S\gamma_1\, C\gamma_3] & [-C\gamma_2\, S\gamma_1\, S\gamma_3 + C\gamma_1\, C\gamma_3] & S\gamma_2\, S\gamma_3 \\ S\gamma_2\, C\gamma_1 & S\gamma_2\, S\gamma_1 & C\gamma_2 \end{pmatrix} , \tag{D1}$$

and we employed the economic notation $Cx=\cos x$ and $Sx=\sin x$.

APPENDIX E: ISOTROPIC REDSHIFT SPACE POWER SPECTRUM IN THE HALO MODEL

The redshift space power spectrum of tracer particles α, can be written in the linear halo model as

$$P^s_\alpha(\mathbf{k}) = P^s_{\alpha,1{\rm H}}(\mathbf{k}) + P^s_{\alpha,2{\rm H}}(\mathbf{k}) \ : \tag{E1}$$

$$P^s_{\alpha,1{\rm H}}(\mathbf{k}) = \frac{P^s_{\alpha,1{\rm H}}(\mathbf{k}|R)}{\left[W(k|R)\right]^2} = \frac{1}{\bar\rho^2_\alpha}\int dM n(M)[W_\alpha]^2\left|U^s(\mathbf{k}|M)\right|^2 \ , \tag{E2}$$

$$P^s_{\alpha,2{\rm H}}(\mathbf{k}) = \frac{P^s_{\alpha,2{\rm H}}(\mathbf{k}|R)}{\left[W(k|R)\right]^2} = \frac{1}{\bar\rho^2_\alpha}\int \prod_{i=1}^{2}\Big\{\, dM_i n(M_i)[W_\alpha]_i U^s(\mathbf{k}|M_i)\Big\}\,\frac{P^s_{\rm hc}(\mathbf{k}|M_1,M_2,R)}{\left[W(k|R)\right]^2} \ . \tag{E3}$$

At linear order the redshift space power spectrum of halo seeds is:

$$\begin{aligned} P^s_{\rm hc}(\mathbf{k}|M_1,M_2,R) &= Z_1(\mathbf{k}|M_1,R)Z_1(\mathbf{k}|M_1,R)P_{11}(k) \\ &= [W(kR)]^2 b_1(M_1)b_1(M_2)P_{11}(k)\left\{1+\mu^2\left[\beta_1+\beta_2\right]+\beta_1\beta_2\mu^4\right\} \ ; \quad \beta_i \equiv \frac{f(\Omega)}{b_1(M_i)} \ . \end{aligned} \tag{E4}$$

where $b_0=0$ can be seen from the fact that the halo and density fluctuation fields are by definition mean zero fields and recalling that at linear order $\left\langle \delta^h_1(r|M)\right\rangle = b_0(M)+b_1(M)\left\langle\delta_1(r|M)\right\rangle$. The isotropic redshift space power spectrum is thus

$$\hat P^s_{\alpha,1{\rm H}}(k) = \frac{1}{\bar\rho^2_\alpha}\int dM n(M)[W_\alpha]^2\left|U^\alpha(k|M)\right|^2\mathcal{R}^{(0)}_{1,2}[k\sigma(M)] \tag{E5}$$

$$P^s_{\alpha,2{\rm H}}(k) = \frac{1}{\bar\rho^2_\alpha}\int \prod_{i=1}^{2}\left\{dM_i n(M_i)b_1(M_i)[W_\alpha]_i U(k|M_i)\right\}\mathcal{R}^{(0)}_{2,2}[k\sigma_2(M)] \tag{E6}$$

where we have defined the redshift space multipole factors

$$\mathcal{R}^{(l)}_{1,n}[a] = \frac{2l+1}{2}\int_{-1}^{1} d\mu \mathcal{P}_l(\mu)\exp\left[-a^2\mu^2\right] \ ; \tag{E7}$$

$$\mathcal{R}^{(l)}_{2,n}[b] = \frac{2l+1}{2}\int_{-1}^{1} d\mu \mathcal{P}_l(\mu)\left[1+A\mu^2+B\mu^4\right]\exp\left[-b^2\mu^2\right] \ . \tag{E8}$$

Here $a^2 \equiv nk^2\sigma^2(M)/2$, ; $b^2 \equiv k^2\left[\sigma^2(M_1)+\cdots+\sigma^2(M_n)\right]/2$ we have set $A=\beta_1+\beta_2$ and $B=\beta_1\beta_2$, and we have assumed our Gaussian model for the 1-pt velocity distribution function from Eq. (B13). Thus, the monopole $[l=0;\,\mathcal{P}_0(\mu)=1]$ moments are

$$\mathcal{R}^{(0)}_{1,n}(a) = \frac{\sqrt{\pi}}{2}\frac{\rm erf[a]}{a} \ ; \tag{E9}$$

$$\mathcal{R}^{(0)}_{2,n}(b) = \frac{\mathcal{R}^{(0)}_{1,n}(b)}{4b^4}\left[4b^4+2b^2A+3B\right] - \frac{\exp(-b^2)}{4b^4}\left[2b^2(A+B)+3B\right] \tag{E10}$$

Our expression differs from that of [39, 40], but is consistent with the formulation of [41]. For further discussion and comments on this subject, and for an evaluation of the power spectrum to higher order in the Halo-PT series, see [42].

Note that when $a \ll 1$ and $b \ll 1$, then

$$\mathcal{R}^{(0)}_{1,n}(a) = \exp(-a^2)\sum_{j=0}^{\infty}\frac{2^j}{(2j+1)!!}\,a^{2j} = \sum_{j=0}^{\infty}\frac{(-1)^j}{j!(2j+1)}\,a^{2j} \tag{E11}$$

$$\begin{aligned}\mathcal{R}^{(0)}_{2,n}(b) &= \frac{\exp(-b^2)}{4b^4}\left(\left[4b^4+2b^2A+3B\right]\sum_{j=0}^{\infty}\frac{2^j}{2j+1)!!}\,b^{2j} - 2b^2(A+B) - 3B\right)\\ &= \frac{\exp(-b^2)}{4b^4}\left(\left[4b^4+2b^2A+3B\right]\left[1+\frac{2b^2}{3}+\frac{4b^4}{15}+\frac{8b^6}{105}+\ldots\right] - 2b^2(A+B) - 3B\right)\\ &= \exp(-b^2)\left(1+\frac{A}{3}+\frac{B}{5}+\frac{2b^2}{3}\left[1+\frac{A}{5}+\frac{3B}{35}\right]+\frac{4b^4}{15}\left[1+\frac{A}{7}+\frac{B}{21}\right]+\ldots\right)\\ &\approx \left(1+\frac{\beta_1+\beta_2}{3}+\frac{\beta_1\beta_2}{5}\right)\end{aligned} \tag{E12}$$

reducing to the Kaiser formula on large scales [92].

[1] M. Tegmark & the SDSS team, Astrophys. J. **606**, 702 (2004).
[2] S. Cole *et al.*, Mon. Not. R. Astron. Soc. **362**, 505 (2005).
[3] M. Tegmark & the SDSS team, astro-ph/0608632 (2006).
[4] D. J. Eisenstein *et al.*, Astrophys. J. **633**, 560 (2005).
[5] D. Spergel *et al.*, astro-ph/0603449 (2006).
[6] F. Bernardeau, S. Colombi, E. Gaztañga, R. Scoccimarro, Physics Reports **367**, 1 (2002).
[7] J. Fry, E. Gaztañaga, Astrophys. J. **425**, 1 (1993).
[8] J. A. Frieman, E. Gaztañaga, Astrophys. J. , **425**, 392, (1994).
[9] J. N. Fry, Phys. Rev. Lett. **73**, 215 (1994).
[10] J. N. Fry, R. J. Scherrer, Astrophys. J. , **429**, 36 (1994).
[11] E. Gaztañaga, P. Fosalba, Mon. Not. R. Astron. Soc. , **301**, 524 (1998).
[12] R. Scoccimarro, Phys. Rev. D. , **69**, 103513 (2004).
[13] E. Sefusatti, M. Crocce, S. Pueblas, R. Scoccimarro, Phys. Rev. D , **D74**, 023522, (2006).
[14] E. Sefusatti, E. Komatsu, arXiv:0705.0343 (2007)
[15] F. Bernardeau, PRD submitted, (2004). astro-ph/0409224
[16] A. Shirata, Y. Suto, C. Hikage, T. Shiromizu, N. Yoshida, arXiv:0705.1311 (2007)
[17] B. Jain, P. Zhang, arXiv:0709.2375 (2007)
[18] R. Scoccimarro, in preparation (2007)
[19] R. E. Smith, P. I. R. Watts, R. K. Sheth, Mon. Not. R. Astron. Soc. **365**, 214 (2006).
[20] W. Saunders, & The PSC Team, Mon. Not. R. Astron. Soc. **317**, 55, (2000).
[21] M. Colless & The 2dFGRS Team, Mon. Not. R. Astron. Soc. **328**, 1039, (2001).
[22] D. G. York & The SDSS Team, Astron. J. , **120**, 1579 (2000).
[23] D. P. Schneider & The SDSS Team, Astron. J. accepted, arXiv:0704.0806 (2007).
[24] I. Kayo, Y. Suto, R. C. Nichol, J. Pan, I. Szapudi, A. J. Connolly, J. Gardner, B. Jain, G. Kulkarni, T. Matsubara, R. K. Sheth, A. S. Szalay, J. Brinkmann, PASJ, **56**, 415, (2004).
[25] Y. P. Jing, G. Böerner, Astrophys. J. , **607**, 140, (2004).
[26] Y. Wang, X. Yang, H. J. Mo, F. C. van den Bosch, Y-Q. Chu, MNRAS, **353**, 287, (2004).
[27] E. Gaztanaga, P. Norberg, C. M. Baugh, D. J. Croton, MNRAS, **364**, 620 (2005).
[28] R. C. Nichol & The SDSS Team, MNRAS, **368**, 1507, (2006).
[29] G. Kulkarni, R. Nichol, R. K. Sheth, et al. Astrophys. J. , in preparation (2007).
[30] H. Feldman, J. Frieman, J. N. Fry, R. Scoccimarro, Phys. Rev. Lett. **86**, 1434 (2001).
[31] L. Verde, A. F. Heavens & The 2dfGRS team, Mon. Not. R. Astron. Soc. , **335**, 432, (2002).
[32] T. Nishimichi, I. Kayo, C. Hikage, K. Yahata, A. Taruya, Y.-P. Jing, R. K. Sheth, Y. Suto, PASJ submitted, astro-ph/0609740 (2006).
[33] R. Scoccimarro, H. M. P. Couchman, J. A. Frieman, Astrophys. J. , **517**, 531, (1999)
[34] E. Gaztañaga, R. Scoccimarro, MNRAS, **361**, 824 (2005).
[35] L. Verde, A. F. Heavens, S. Matarrese, L. Moscardini, Mon. Not. R. Astron. Soc. , **300**, 747(1998).
[36] R. E. Smith, R. Scoccimarro, R. K. Sheth, Phys. Rev. D , 75.063512, (2007).
[37] A. Cooray, R. K. Sheth, Physics Reports, **372**, 1 (2002).
[38] R. K. Sheth, A. Diaferio, L. Hui, R. Scoccimarro, Mon. Not. R. Astron. Soc. **326**, 463 (2001).
[39] M. White, Mon. Not. R. Astron. Soc. , **321** 1, (2001).
[40] U. Seljak, Mon. Not. R. Astron. Soc. , **325** 1359, (2001).
[41] X. Kang, Y. P. Jing, H. J. Mo, G. Böerner, Mon. Not. R. Astron. Soc. , **336** 892, (2002).
[42] R. E. Smith, R. Scoccimarro, R. K. Sheth, in preparation, (2008)

[43] A. J. Benson, S. Cole, C. S. Frenk, C. M. Baugh, C. G. Lacey, Mon. Not. R. Astron. Soc. , **311**, 793, (2000).

[44] U. Seljak, Mon. Not. R. Astron. Soc. , **318**, 203 (2000).

[45] J. A. Peacock, R. E. Smith, Mon. Not. R. Astron. Soc. **318**, 1144 (2000).

[46] R. Scoccimarro, R. K. Sheth, L. Hui, B. Jain, Astrophys. J. **546**, 20 (2001).

[47] A. Berlind, D. Weinberg, Astrophys. J. **575**, 587 (2002).

[48] R. E. Smith, J. A. Peacock, A. Jenkins, S. D. M. White, C. S. Frenk, F. R. Pearce, P.A. Thomas, G. Efstathiou H. M. P. Couchman, Mon. Not. R. Astron. Soc. **341**, 1311 (2003).

[49] M. Crocce, R. Scoccimarro, arXiv:0704.2783 (2007).

[50] M. C. Neyrinck, I. Szapudi, Mon. Not. R. Astron. Soc. submitted (2007). astro-ph/arXiv:0710.3586.

[51] U. Seljak, M. Zaldarriaga, Astrophys. J. **469**, 437 (1996).

[52] R. Scherrer, E. Bertschinger, Astrophys. J. , **381**, 349 (1991).

[53] M. Takada, B. Jain, Mon. Not. R. Astron. Soc. , **340**, 580, (2003).

[54] W. Press, P. Schechter, Astrophys. J. , **187**, 425, (1974)

[55] J. R. Bond, S. Cole, N. Kaiser, G. Efstathiou, Astrophys. J. , **379**, 440, (1991).

[56] R. K. Sheth, G. Tormen, Mon. Not. R. Astron. Soc. **308**, 119 (1999).

[57] R. K. Sheth, H.-J. Mo, B. Tormen, Mon. Not. R. Astron. Soc. , **323**, 1, (2001).

[58] A. Jenkins, C. S. Frenk, S. D. M. White, J. Colberg, S. Cole, A. Evrard, H. Couchman N. Yoshida, Mon. Not. R. Astron. Soc. , **321**, 372, (2001).

[59] M. S. Warren, K. Abazajian, D. E. Holz, L. Teodoro, astro-ph/0604310 (2005).

[60] D. Reed, R. Bower, C. S. Frenk, A. Jenkins, T. Theuns, Mon. Not. R. Astron. Soc. , **374**, 2 (2007).

[61] Moore B., Quinn T., Governato F., Stadel J., Lake G., 1999. MNRAS, 310, 1147

[62] Klypin A., Gottlber S., Kravtsov A., Khokhlov A. M., 1999. ApJ, 516, 530

[63] Jing Y. P., Suto Y., 2002. ApJ, 574, 538. (JS02)

[64] Benson A. J., Mon. Not. R. Astron. Soc. , **358**, 551 (2005).

[65] R. E. Smith, P. I. R. Watts, Mon. Not. R. Astron. Soc. **360**, 203 (2005).

[66] E. Hivon, F. R. Bouchet, S. Colombi, R. Juszkiewicz, Astron. Astrophys. , **298**, 643 (1995)

[67] P. McDonald, astro-ph/0609413 (2006).

[68] P. J. E. Peebles, *"The Large-scale Structure of the Universe"* (Princeton University Press, Princeton, 1980.)

[69] R. Scoccimarro, Mon. Not. R. Astron. Soc. , **299**, 1097 (1998).

[70] M. Crocce, S. Pueblas, R. Scoccimarro, Mon. Not. R. Astron. Soc. , **373**, 369 (2006).

[71] V. Springel, Mon. Not. R. Astron. Soc. , **364**, 1105 (2005).

[72] R. W. Hockney, J. W. Eastwood,"Computer Simulations Using Particles", McGraw-Hill, New York (1981).

[73] M. Frigo, S. G. Johnson, `http://www.fftw.org/` (2007).

[74] Y. P. Jing, Astrophys. J. , **620**, 559 (2005).

[75] R. Scoccimarro, S. Colombi, J. N. Fry, J. A. Frieman, E. Hivon, A. Melott, Astrophys. J. , **517**, 531, (1999)

[76] R. Angulo, C. M. Baugh, C. S. Frenk, C. G. Lacey, Mon. Not. R. Astron. Soc. , submitted astro-ph/0702543 (2007).

[77] D. J. Eisenstein, W. Hu, Astrophys. J. , **496**, 605 (1998).

[78] A. Meiksin, M. White, J. A. Peacock, Mon. Not. R. Astron. Soc. , **304**, 851 (1999).

[79] R. E. Smith, R. Scoccimarro, R. K. Sheth, Phys. Rev. D submitted, (2007b). astro-ph/0703620

[80] R. Scoccimarro, Phys. Rev. D. , **70**, 083007 (2004).

[81] I. Szapudi, Astrophys. J. , **605**, L89, (2004).

[82] Z. Zheng, Astrophys. J. , **614**, 527, (2004).

[83] P. Fosalba, J. Pan, I. Szapudi, Astrophys. J. , **632**, 29 (2005)

[84] J. Navarro, C. S. Frenk, S. D. M. White, Astrophys. J. **490**, 493 (1997). (NFW)

[85] G. Bryan, M. Norman, Astrophys. J. , **495**, 80, (1998).

[86] J. Bullock, T. Kolatt, Y. Sigad, R. Somerville, A. Kravtsov, A. Klypin, J. Primack, A. Dekel, Mon. Not. R. Astron. Soc. , **321**, 559, (2001).

[87] O. Lahav, P. Lilje, J. Primack, M. Rees, Mon. Not. R. Astron. Soc. , **251**, 128

[88] R. K. Sheth, B. Jain, Mon. Not. R. Astron. Soc. , **345**, 592 (2003).

[89] R. K. Sheth, Mon. Not. R. Astron. Soc. , **279**, 1310, (1996).

[90] J. Binney, S. Tremaine, *Galactic Dynamics*, Princeton University Press, Princeton, USA, (1988).

[91] Mathews J, Walker R. L., 1970. *"Mathematical methods of physics"*, W. A. Benjamin Publishers Inc., New York

[92] N. Kaiser, Mon. Not. R. Astron. Soc. , **227**, 1, (1987).

[93] This model neglects many aspects of the more complex physics that, we understand from high resolution N-body simulations, play an important role in the internal dynamics of dark matter haloes. For example: the presence of merged substructures will produce significant localized structure in the phase space distribution [61, 62]; a global asymmetry of the underlying potential generated through the anisotropic accretion of matter by the halo will distort the velocity structure of the phase space into a 6-D ellipsoid [63, 64]